Modelling C_1-C_4 alkyl nitrate photochemistry and their impacts on O_3 production in urban and suburban environments of Hong Kong

X.P. Lyu [1], H. Guo * [1], N. Wang [2], I.J. Simpson [3], H.R. Cheng ** [4], L.W. Zeng[1], S. Meinardi [3], and D.R. Blake [3]

[1] Department of Civil and Environmental Engineering, The Hong Kong Polytechnic University, Hong Kong

[2] Guangdong Provincial Key Laboratory of Regional Numerical Weather Prediction, Institute of Tropical and Marine Meteorology, Guangzhou, China

[3] Department of Chemistry, University of California at Irvine, Irvine, CA, USA

[4] Department of Environmental Engineering, Wuhan University, Wuhan, China

* First corresponding author: ceguohai@polyu.edu.hk

** Second corresponding author: chenghr@whu.edu.cn

Keywords: organic nitrate, odd nitrogen, ozone, photochemical smog, MCM

Abstract: As intermediate products of photochemical reactions, alkyl nitrates ($RONO_2$) regulate ozone (O_3) formation. In this study, a photochemical box model (PBM) incorporating master chemical mechanism (MCM) well reproduced the observed $RONO_2$ at an urban and a mountainous site, with index of agreement (IOA) all higher than 0.65. Although levels of the parent hydrocarbons and nitric oxide (NO) were significantly higher at the urban site than the mountainous site, the production of C_2-C_3 $RONO_2$ was comparable to or even lower than at the mountainous site, due to the lower photochemical reactivity in the urban environment. Based on the profiles of air pollutants at the mountainous site, the formation of C_2-C_4 $RONO_2$ was limited by NO_x (VOCs) when TVOCs/NO_x was higher (lower) than 3.3/1 ppbv/ppbv. However, the threshold of this ratio increased to 8.1/1 ppbv/ppbv at the urban site. For the formation of C_1 $RONO_2$, the NO_x limited regime extended the ratio of TVOCs/NO_x to as low as 1.8/1 and 3.0/1 ppbv/ppbv at the mountainous and urban site, respectively. $RONO_2$ formation led to a decrease of simulated O_3, with reduction efficiencies (O_3 reduction/$RONO_2$ production) of 4-5 pptv/pptv

at the mountainous site, and 3-4 pptv/pptv at the urban site. On the other hand, the variations of simulated O_3 induced by $RONO_2$ degradation depended upon the regimes controlling O_3 formation and the relative abundances of TVOCs and NO_x.

1 Introduction

Alkyl nitrates ($RONO_2$) are a group of organic nitrates in which the nitrogen is stabilized in the molecular structure of R-O-NO_2. As an important constituent of reactive odd nitrogen (NO_y), particularly in areas far from urban sources (Roberts and Fajer, 1989; Buhr et al., 1990), $RONO_2$ participate in nitrogen cycling in their role as a temporary nitrogen reservoir due to their long atmospheric lifetimes (Clemitshaw et al., 1997). Generally, oceanic emission (Atlas et al., 1993), photochemical formation (Bertman et al., 1995; Arey et al., 2001), and to a lesser extent biomass burning (Simpson et al., 2002) are the main sources of $RONO_2$. The photochemically formed $RONO_2$ are actually byproducts in the process of O_3 formation (Reactions 2 and 3), and are formed through the reactions between volatile organic compounds (VOCs) and nitrogen oxides (NO_x) (Reaction 1 and 4). These combined formation pathways, as a result, generally lead to the tight association between $RONO_2$ and O_3 (Muthuramu et al., 1994; Rosen et al., 2004).

Many formation mechanisms have been proposed to explain observed $RONO_2$ levels in urban settings, including RO_2 reacting with NO (Darnall et al., 1976; Carter and Atkinson, 1989) and RO reacting with NO_2 (Atkinson et al., 1982a), which well documented and play dominant roles in $RONO_2$ formation, particularly in daytime hours. For the reactions of RO_2+NO, two branches exist, leading to the formation of $RONO_2$ (Reaction 1) and O_3 (Reaction 2), respectively (Atkinson, 1990). The branching ratio (α) is a quantitative measure of $RONO_2$ yield from RO_2 reacting with NO. It is defined as the ratio of $k_1/(k_1+k_2)$ (Atkinson, 1990), where k is the reaction rate constant. Generally, the branching ratio increases with increasing pressure and decreasing temperature (Atkinson et al., 1987). In addition, more complicated molecular structures of RO_2 tend to have higher branching ratios. For example, the branching ratios for *n*-alkanes increase from ≤1% for ethane to ~33% for *n*-octane, with an upper limit of ~35% for larger *n*-alkanes (Atkinson et al., 1982a). This theory was repeatedly confirmed by kinetic calculations and model simulations (Bertman et al., 1995; Simpson et al., 2006). In combination with laboratory studies, Carter and Atkinson (1985) put forward Formulas 1-3 for calculating branching ratios under the atmospheric conditions in troposphere. However, in urban settings the smaller-chain $RONO_2$,

particularly methyl (CH_3ONO_2) and ethyl nitrate ($C_2H_5ONO_2$), often have mixing ratios higher than what can be explained by the reaction of RO_2 with NO (Flocke et al., 1998a). Depending on the location, direct marine emissions could be one reason (Atlas et al., 1993). In addition, the exact branching ratios for these $RONO_2$ remain uncertain. For example, Lightfoot et al. (1992) proposed an upper limit of 0.005 for CH_3ONO_2 in the lower troposphere. Through $RONO_2$ observations in the lower stratosphere, Flocke et al. (1998b) found a much lower CH_3ONO_2 branching ratio of $5\text{-}10\times10^{-5}$, meaning it could only reach a maximum of 0.0003 even under surface conditions, when applying the adjusted factor of 3 to the branching ratio in lower stratosphere. Simpson et al. (2002) accepted the upper limit of 0.0003, and indicated that RO reacting with NO_2 was the main pathway of CH_3ONO_2 in highly polluted environments. However, according to the formulas proposed by Carter and Atkinson (1985), the branching ratio for CH_3ONO_2 was approximately 0.001, which was also adopted by the master chemical mechanism (MCM, accessible at http://mcm.leeds.ac.uk/MCM/). Overall, the branching ratios for $RONO_2$ formation remain to be further examined.

$RO_2 + NO \rightarrow RONO_2$ (Reaction 1, k_1)

$RO_2 + NO \rightarrow RO + NO_2$ (Reaction 2, k_2)

$NO_2 + O_2 \rightarrow NO + O_3$ (Reaction 3, k_3)

$RO + NO_2 \rightarrow RONO_2$ (Reaction 4, k_4)

$$\alpha = \left[\frac{Y_0^{300}[M]\left(\frac{T}{300}\right)^{-m_0}}{1+\frac{Y_0^{300}[M]\left(\frac{T}{300}\right)^{-m_0}}{Y_\infty^{300}\left(\frac{T}{300}\right)^{-m_\infty}}}\right]F^z \quad \text{(Formula 1)}$$

$$z = \left\{1 + \left[\log\frac{Y_0^{300}[M]\left(\frac{T}{300}\right)^{-m_0}}{Y_\infty^{300}\left(\frac{T}{300}\right)^{-m_\infty}}\right]^2\right\}^{-1} \quad \text{(Formula 2)}$$

$$Y_0^{300} = \beta e^{\gamma n} \quad \text{(Formula 3)}$$

where T is the temperature (K); M represents the number of molecules (molecules/cm^3) and n is the carbon number in RO_2. The values of the constants β (1.95×10^{-22} cm^3/molecule), γ (0.947), Y_∞^{300} (0.435), m_0 (2.99), m_∞ (4.69) and F (0.556) are all from Carter and Atkinson (1985). On the basis of the calculated results, the branching ratios for the primary and tertiary RO_2 radicals

are calibrated by a factor of 0.4 and 0.25, respectively. For C_1 $RONO_2$, another adjusted factor of 3 should be further applied to formula 1.

It is well known that O_3 formation is closely related to the relative abundances of VOCs and NO_x, mainly due to the dual role of NO_x in O_3 production (*i.e.*, fueling and suppressing O_3 formation in low and high NO_x regimes, respectively) (Sillman and He, 2002; Shao et al., 2009). As byproducts of O_3 formation, the production of $RONO_2$ is also expected to be influenced by the abundances of VOCs and NO_x. However, there is no evidence that NO_x directly reacts with $RONO_2$ in the same way as the titration of NO to O_3. Instead, NO reacts with the hydroperoxyl radical (HO_2) and RO_2, and NO_2 combines with hydroxyl radical (OH), to regulate the equilibrium budgets of oxidative radicals including RO_2 and RO (Thornton et al., 2002). As such, the $RONO_2$ production will be influenced by NO_x. It was found that $RONO_2$ levels increased with increasing NO_x in London (Aruffo et al., 2014), but decreased with increasing NO_x in Houston (Rosen et al., 2004), suggesting a different balance in HO_x-NO_x reaction cycles. Therefore, the relationship between $RONO_2$ production and NO_x needs further study.

Due to the associated formation pathways of $RONO_2$ and O_3, good correlations are often found between single or total $RONO_2$ ($\sum$ANs) and O_3 or O_x (O_x=O_3+NO_2) (Rosen et al., 2004; Perring et al., 2010). A roughly quantitative relationship can be established between O_x and $\sum$ANs, *i.e.*, $O_x/\sum ANs = 2(1-\alpha)/\alpha$ (Day et al., 2003), where α represents the overall branching ratio for the total $RONO_2$. More importantly, $RONO_2$ photochemistry, including their formation and degradation (photolysis and OH initiated oxidation) also influences O_3 formation. Based on correlations between O_x and $\sum$ANs, Aruffo et al. (2014) stated that $RONO_2$ played important roles in O_3 formation in both urban and suburban London. Perring et al. (2010) indicated that the peak O_3 production in the near-field of Mexico City (source region of $RONO_2$) was reduced by as much as 40% due to the formation of total $RONO_2$. Farmer et al. (2011) even claimed that VOC reductions might cause an O_3 increment because the branching ratios of $RONO_2$ formation decreased when fuels containing low boiling point VOCs products were used. This view was also confirmed by Perring et al. (2013), in which a 20% reduction of VOCs led to an 8% O_3 increment due to the unexpected reduction of the average branching ratio for total $RONO_2$ from 8% to 4%. Overall, in urban areas $RONO_2$ serve as a reservoir for nitrogen and reactive radicals,

112 releasing them in remote areas and fueling O_3 formation. Therefore, $RONO_2$ photochemistry
113 regulates O_3 formation in both source and receptor regions.

114 Despite numerous studies, $RONO_2$ modelling is still rather difficult (Williams et al., 2014; Khan
115 et al., 2015), resulting in an insufficient understanding of $RONO_2$ formation mechanisms and
116 impacts on O_3 production. Furthermore, previous studies are generally confined to specific
117 $RONO_2$ species, like CH_3ONO_2 in marine outflow (Flocke et al., 1998b; Moore and Blough,
118 2002) and isoprene nitrates in the forest areas (Chen et al., 1998; Giacopelli et al., 2005). To fill
119 in these research gaps, an observation-based model was constructed to explicitly simulate C_1-C_4
120 $RONO_2$ in Hong Kong and address the following terms: (1) the most appropriate branching
121 ratios for the formation of C_1-C_4 $RONO_2$ in Hong Kong; (2) the pathway contributions of
122 RO_2+NO and RO+NO_2 to $RONO_2$; (3) the relationship between $RONO_2$ production and NO_x; (4)
123 the impacts of $RONO_2$ formation and degradation on O_3 production; and (5) the importance of
124 $RONO_2$ formed from parent hydrocarbons with high O_3 formation potentials.

125 **2. Methodology**

126 **2.1 Site description and sampling**

127 From September 6 to November 29, 2010, an intensive sampling campaign was carried out
128 concurrently at a mountainous site and an urban site in Hong Kong (Figure 1). The mountainous
129 site (22.41 N °, 114.12 E °, 640 m a.g.l.) was located on the mountainside of Hong Kong's highest
130 mountain (Mount. Tai Mo Shan), referred to as TMS hereafter. The dominant winds at TMS
131 were from the north which transported air pollutants from the inland Pearl River Delta (PRD) of
132 southern China. In addition, mesoscale circulation (*e.g.*, mountain-valley breezes) caused
133 interaction of mountainous air with urban plumes at the foot of the mountain. The urban site
134 (22.37 N °, 114.11 E °, 10 m a.g.l.) is located in a newly developed town (Tsuen Wan, referred to
135 TW hereafter), and is an air quality monitoring station of Hong Kong Environmental Protection
136 Department (HKEPD, accessible at http://www.aqhi.gov.hk/en/monitoring-network/air-quality-
137 monitoring-stations228e.html?stationid=77). The prevailing winds at TW were from the
138 southeast. Detailed information about the two sites is given in Guo et al. (2013) and Ling et al.
139 (2014, 2016).

Real time measurements of trace gases including SO_2, CO, NO, NO_2 and O_3 at TMS were achieved with the instruments listed in Table S1 of the Supplement, which also shows the analytical techniques, detection limits and precision. Trace gas data at TW were downloaded from the HKEPD website (http://epic.epd.gov.hk/EPICDI/air/station/). VOC samples at these two sites were collected using 2-L electro-polished stainless steel canisters. Prior to sampling, the canisters were treated with 10 Torr of degassed, distilled water to quench the active surface sites of the inner walls, then were cleaned and evacuated. A valve was connected to the inlet of the canisters to maintain a sampling time of about 1 hour. A total of 384 samples were simultaneously collected during daytime hours of 10 O_3 episode days (October 23-24, 29-31, and November 1-3, 9, 19, 2010) and 10 non-O_3 episode days (September 28, October 2, 8, 14, 18-19, 27-28 and November 20-21, 2010) at TMS and TW, except those samples not collected at TW on October 23. In this study, days with at least one hourly O_3 mixing ratio exceeding 100 ppbv were defined as O_3 episode days (China's Grade II standards, accessible at http://210.72.1.216:8080/gzaqi/Document/gjzlbz.pdf). The O_3 values at TMS were used to define the O_3 episodes and non-episodes, because freshly-emitted NO from vehicular exhaust strongly titrated O_3 at TW (Guo et al., 2013).

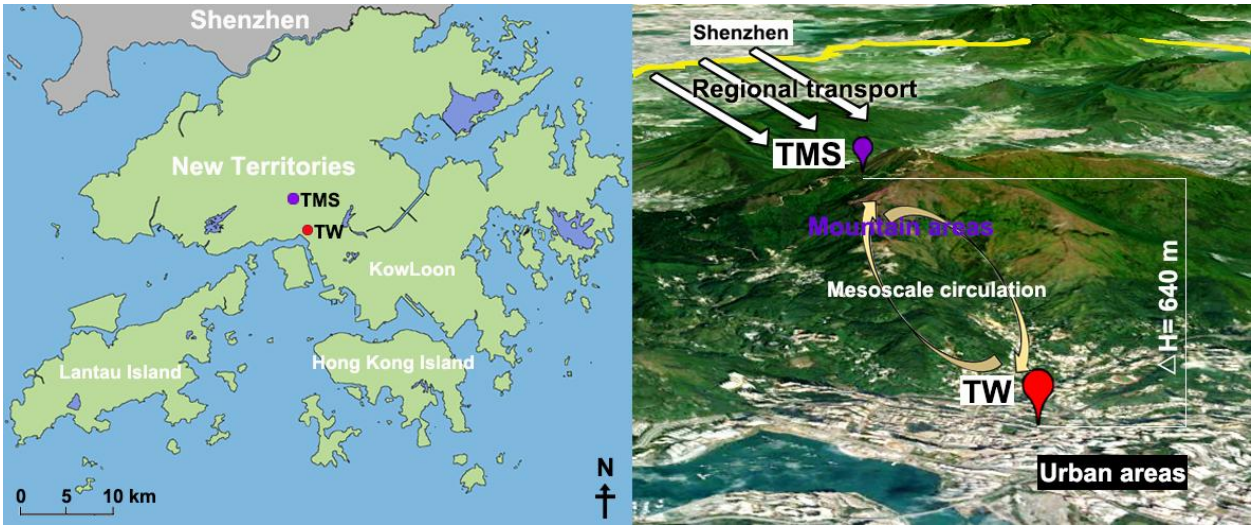

Figure 1 Geographic locations (left panel) and topographies (right panel) of the sampling sites (TMS and TW). Regional transport and mesoscale circulation at TMS are presented according to Guo et al. (2013). The boundary between mainland China and Hong Kong is highlighted in yellow.

2.2 Chemical analysis of $RONO_2$

The collected VOC samples were delivered to the Rowland/Blake group at the University of California, Irvine (UCI) for chemical analyses. Detailed descriptions about the analytical system, analysis techniques, precision, accuracy, and quality control protocols can be found in Colman et al. (2001) and Simpson et al. (2003).

Specifically, for the quantification of C_1-C_4 $RONO_2$, *i.e.*, methyl nitrate (CH_3ONO_2 or C_1 $RONO_2$), ethyl nitrate ($C_2H_5ONO_2$ or C_2 $RONO_2$), *i*-propyl nitrate (2-$C_3H_7ONO_2$ or 2-C_3 $RONO_2$), *n*-propyl nitrate (1-$C_3H_7ONO_2$ or 1-C_3 $RONO_2$) and *sec*-butyl nitrate (2-$C_4H_9ONO_2$ or 2-C_4 $RONO_2$), a gas chromatography (GC)-electron capture detector (ECD) system was used. Two whole air working standards were analyzed every four samples to calibrate the $RONO_2$ measurements. The precision was 2% for mixing ratios above 5 pptv and 10% for mixing ratios below 5 pptv. The accuracy was 10-20%and the detection limit for C_1-C_4 $RONO_2$ was 0.01 pptv. It is worth noting that the $RONO_2$ calibration scale changed in 2008 (Simpson et al., 2011) and all measurements are reported on the new calibration scale.

2.3 Construction of PBM-MCM model

A PBM-MCM model was developed to simulate $RONO_2$. Master Chemical Mechanism (MCM) is an explicit chemical mechanism, which has been successfully used in photochemical simulation in Hong Kong and many other regions of the world (Saunders et al., 2003; Lam et al., 2013; Ling et al., 2014). The latest version of MCM (MCM v3.3) includes 17,242 reactions and 5,836 species. With regards to $RONO_2$, the main formation pathways that are considered are RO_2+NO and RO+NO_2, while $RONO_2$ degradation is presented as photolysis (reaction 5) and OH initiated oxidation (reaction 6). Details about the reaction pathways and reaction coefficients are given in Section S1 of the Supplement.

$RONO_2 + h\nu \rightarrow RO + NO_2$ (reaction 5)

$RONO_2 + OH \rightarrow RO + NO_2 +$ products (reaction 6)

The branching ratios for the reactions of RO_2+NO were acquired from previous studies (Lightfoot et al., 1992; Flocke et al., 1998b) or calculated according to the formulas recommended by Carter and Atkinson (1985). For C_1 $RONO_2$, branching ratios of 0.00015,

0.0003, 0.001, 0.003, 0.0041 and 0.005 were examined and considered. However, since branching ratio data for C_2-C_4 $RONO_2$ were rather limited, the values calculated using formulas 1-3 were used as the branching ratios, which were 0.0094, 0.048, 0.019 and 0.085 for C_2, 2-C_3, 1-C_3 and 2-C_4 $RONO_2$, respectively. Bearing in mind model uncertainty, the branching ratios were accepted only when IOAs between the simulated and observed $RONO_2$ were higher than 0.65 (see section 3.1 for details).

In addition to the chemical reactions, many modules were compiled in the PBM-MCM model. For example, the photolysis rate module enables us to calibrate the photolysis rates of many air pollutants. The Tropospheric Ultraviolet and Visible Radiation (TUVv5) model, which considers actual location and modelling time periods, is used to calibrate the photolysis rates (Madronich and Flocke, 1997). Moreover, the concentrations of air pollutants can be specified to initiate the model in the initial concentration module. This is important, because the background $RONO_2$ existed prior to photochemical reactions are generally non-negligible due to their long lifetimes. In this study, $RONO_2$ mixing ratios observed at 07:00 (local time, LT) were treated as the initial conditions. The dry deposition module considers the dry deposition of air pollutants, which are parameterized as an average deposition rate within the height of the mixed layer (HMIX). Zhang et al. (2002) indicated that the dry deposition velocity for organic nitrates ranged from 0.03 to 0.56/HMIX cm/s. Within this range, deposition rates of 0.03, 0.13, 0.23, 0.33, 0.43 and 0.53/HMIX cm/s were examined for C_1-C_4 $RONO_2$ in this study (step=0.1/HMIX cm/s).

Overall, based on the observed mixing ratios of air pollutants, including $RONO_2$ precursors, the PBM-MCM model simulated $RONO_2$ in different scenarios with changes of branching ratios and dry deposition rates, and consideration of initial conditions. The model uncertainty was discussed and roughly estimated with the mean root square error method (Willmott, 1982) in Section S2 of the Supplement.

3 Results and discussion

3.1 Modelling of C_1-C_4 $RONO_2$

The abundance, day-to-day variation, chemical evolution and sources of C_1-C_4 $RONO_2$ at TMS and TW were discussed in Ling et al. (2016). One of their key findings was that secondary

formation (or photochemical formation) was the main contributor of $RONO_2$ at both sites, but the formation mechanisms remained unexplained, which were studied in this section.

Figure 2(a) shows the average photochemical production of CH_3ONO_2 at TMS as a function of the branching ratio (Section 2.3), without consideration of initial concentrations and dry deposition. Noticeably, the CH_3ONO_2 production linearly increases with increasing branching ratio (CH_3ONO_2 mixing ratio in pptv = (4400 × branching ratio) + 1.4). A branching ratio of approximately 0.0023 was determined to match the observed CH_3ONO_2 (11.3 pptv). This branching ratio was within the range of 0.00015 to 0.005 as reported earlier (Carter and Atkinson, 1985; Lightfoot et al., 1992; Flocke et al., 1998b). However, the initial mixing ratio (8.8 pptv) was not considered in Figure 2(a), which should also be a part of the observed CH_3ONO_2 even though it was subject to degradation and dry deposition. Even taking into account the degradation (OH initiated oxidation and photolysis) and dry deposition (rate = 0.13/HMIX cm/s), the average residual of the initial CH_3ONO_2 was still 7.5 pptv. Based on this value, photochemically formed CH_3ONO_2 was about 3.8 pptv, which corresponded to a branching ratio of 0.00055, also within the range of 0.00015-0.005. However, this value was calculated based on model simulation rather than laboratory experiment and has never been reported in previous studies. Therefore, we adopted a branching ratio of 0.0003, reported by Flocke et al. (1998b) and adopted by Simpson et al. (2002), which was the closest to 0.00055 among the examined values. Furthermore, by considering dry deposition, Figure 2(b) presents the modelled CH_3ONO_2 with the branching ratio of 0.0003 and dry deposition velocities of 0.03/HMIX, 0.13/HMIX, 0.23/HMIX, 0.33/HMIX, 0.43/HMIX and 0.53/HMIX cm/s. The modelled CH_3ONO_2 decreased linearly with increasing dry deposition velocity (CH_3ONO_2 mixing ratio in pptv = -4.5 × deposition rate + 11.6). A dry deposition velocity of 0.07/HMIX was determined to best reproduce the observed CH_3ONO_2. As such, the branching ratio of 0.0003 and dry deposition velocity of 0.07/HMIX cm/s were treated as the most appropriate settings for CH_3ONO_2 simulation.

With these settings, the factors influencing the simulated CH_3ONO_2 were sequentially considered. Figure 3 shows the CH_3ONO_2 simulated in different scenarios at TMS, *i.e.*, (*i*) "reaction", (*ii*) "reaction + initial" and (*iii*) "reaction + initial + dry deposition". Scenario (*i*) only considered the formation and degradation reactions of CH_3ONO_2, while the initial concentrations

and dry deposition were progressively considered in scenarios (*ii*) and (*iii*). The modelled CH_3ONO_2O in scenario (*i*) was typically bell-shaped on a diurnal basis, coincident with the characteristics of photochemical reactions. However, the mean modelled CH_3ONO_2 (2.6 ± 0.3 pptv) was much lower than the observed average (11.3 ± 0.3 pptv). By introducing the initial conditions, the modelled CH_3ONO_2 in scenario (*ii*) increased to a comparable level (11.7 ± 0.3 pptv) to the measurements, in line with the finding that background initial concentrations are an important constituent of the observed $RONO_2$ (Ling et al., 2016). Further consideration of dry deposition in scenario (*iii*) resulted in a slight decrease of the modelled CH_3ONO_2 to 11.0 ±0.3 pptv, which best agreed with the observed CH_3ONO_2. By subtracting the modelled CH_3ONO_2 in scenario (*i*) from scenario (*ii*) and that in scenario (*ii*) from scenario (*iii*), the respective contributions of the processes, including reaction, initial conditions and dry deposition to the total modelled CH_3ONO_2, were determined to be 21.5 ± 1.8%, 85.1 ± 2.0% and -6.6 ±0.3% (negative contribution means removal of CH_3ONO_2).

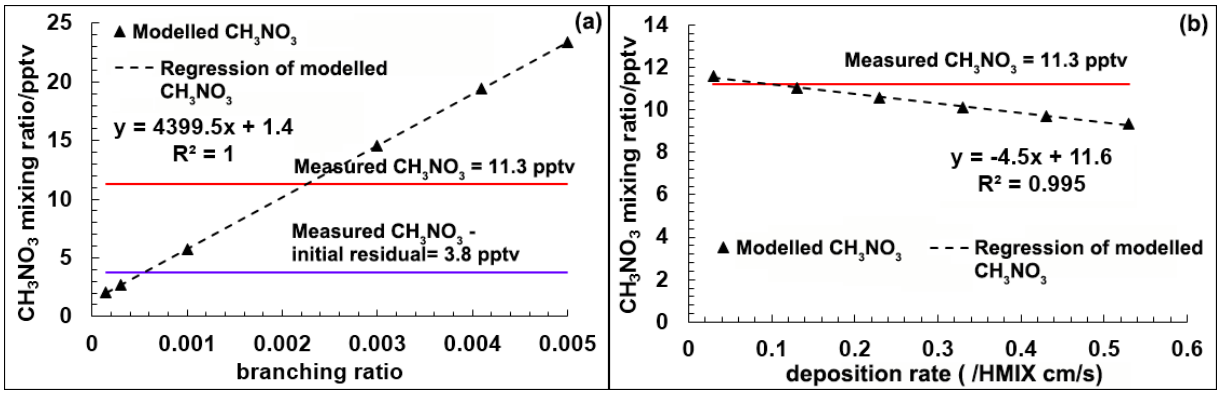

Figure 2 Modelled average CH_3ONO_2 as a function of (a) branching ratio (no initial or dry deposition) and (b) deposition rate (branching ratio = 0.0003, and the initial CH_3ONO_2 was set as the values measured at 07:00 (LT) at TMS for each day.

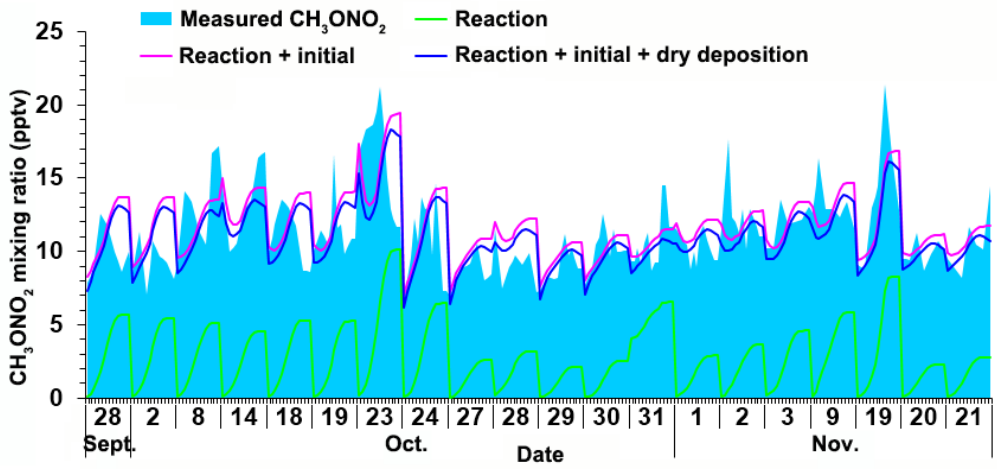

Figure 3 Comparisons between the measured and modelled CH_3ONO_2 in different scenarios at TMS.

Similarly, the C_2-C_4 $RONO_2$ were also simulated using the above approach. Table 1 lists the model settings that best reproduced the magnitudes and patterns of the observed $RONO_2$ at TMS and TW (shown in Figures S1-S2 in the Supplement). Overall, the simulated $RONO_2$ agreed well with the measurements (Index of Agreement is discussed below). However, the morning peaks of $RONO_2$ (*e.g.*, September 28, October 8 and 23, and November 1 and 2) were not well reproduced by the model. Since in situ photochemical formation could not be the main source of $RONO_2$ in the morning when solar radiation was weak, the discrepancies between modelling and observation were most likely to be caused by direct emissions and/or regional transport, which were not considered in the model. In addition, the modelled $RONO_2$ levels were generally ~50% lower than the observations on O_3 episode days (October 23-24, 29-31, and November 1-3, 9, 19). Methyl chloride (CH_3Cl) levels at both TMS (episode: 1100 ± 33 pptv; non-episode: 926 ± 27 pptv) and TW (episode: 1116 ± 32 pptv; non-episode: 1031 ± 45 pptv) increased noticeably (p<0.05) during O_3 episodes, so did levoglucosan in fine particles (84.8±27.8 and 31.6±18.5 ng/m^3 during episode and non-episode at TMS, respectively). These suggested emissions of $RONO_2$ from biomass burning. Furthermore, the frequency of northerly winds was higher during O_3 episodes (78% at TMS and 29% at TW) than during non-O_3 episodes (51% at TMS and 21% at TW). In view of severe photochemical pollution in the adjacent inland PRD cities and increased transport of secondary pollutants from the inland PRD to Hong Kong during O_3

episodes (Lam et al., 2005; Guo et al., 2009), regional transport might also contribute to the higher observed $RONO_2$ on episode days. An exception was CH_3ONO_2 at TW on November 19 when the modelled CH_3ONO_2 remarkably exceeded the measured values (Figure S2). This overestimation was believed to be caused by the abnormally high aromatic levels on that day (30.2 ± 23.4 ppbv, compared to the average of 4.9 ± 0.6 ppbv over the whole sampling period excluding that day). Briefly, the photochemical degradation of aromatics generated CH_3O_2 and CH_3O in the model. Without consideration of diffusion, these precursors of CH_3ONO_2 were more significantly overestimated than those in normal periods, leading to overestimation of CH_3ONO_2.

To quantitatively evaluate the simulations, IOA between the simulated and observed $RONO_2$ was calculated (Table 1). IOA is a statistical parameter commonly used to evaluate model performance, as calculated using Formula 4 (Hurley et al., 2001). Ranging from 0-1, higher IOAs represent better agreement between the simulated and observed values. We accepted the simulation results when the IOA was above 0.65.

$$IOA = 1 - \frac{\sum_{i=1}^{n}(O_i - S_i)^2}{\sum_{1i=1}^{n}(|O_i - \bar{O}| + |S_i - \bar{O}|)^2} \quad \text{(Formula 4)}$$

where O_i and S_i are the observed and simulated values, and $\bar{O}$ is the average observed value of n samples.

Table 1 Model settings for the simulations of C_1-C_4 $RONO_2$ as well as IOAs between the simulated and measured $RONO_2$ at TMS and TW.

	CH_3ONO_2	$C_2H_5ONO_2$	1-$C_3H_7ONO_2$	2-$C_3H_7ONO_2$	2-$C_4H_9ONO_2$
Branching ratio	0.0003	0.0094	0.019	0.048	0.085
Dry deposition	0.07/HMIX	0.07/HMIX	0.07/HMIX	0.07/HMIX	0.07/HMIX
IOA at TMS	0.67	0.72	0.72	0.72	0.72
IOA at TW	0.66	0.70	0.69	0.67	0.73

HMIX is the time-dependent mixed layer height, as shown in Figure S3.

The IOA ranged from 0.67 to 0.72 and 0.66 to 0.73 for $RONO_2$ simulations at TMS and TW, respectively. Given that other sources (*e.g.*, biomass burning and oceanic emission) and regional

transport impact were not considered in the model, the IOAs indicated that the simulations were acceptable.

3.2 Secondary $RONO_2$ formation

Based on the above settings, the secondary (photochemical) production of $RONO_2$ (referred to as secondary $RONO_2$ hereafter) was simulated without consideration of initial conditions and dry deposition, as summarized in Table 2. Also shown are the concentrations of parent hydrocarbons, corresponding RO_2 radicals, NO and NO_2. The measured mixing ratios of parent hydrocarbons and NO_x (both NO and NO_2) were significantly higher at TW than at TMS ($p<0.05$). Likewise simulated C_1 and 2-C_4 $RONO_2$ levels at TW were significantly higher than at TMS ($p<0.05$), while the simulated C_2 and C_3 $RONO_2$ levels at TW were comparable to or even lower than those at TMS. To explore the reasons for these differences, the relative contributions of RO_2+NO and RO+NO_2 were quantified (Table 3), using the method described by Lyu et al. (2015). Briefly, the two pathways were switched off in turn. The simulated $RONO_2$ was subtracted from that simulated in base scenario with both pathways switched on. In this way, $RONO_2$ produced by the each pathway was obtained. The pathway of RO_2+NO dominated the formation of C_2-C_4 $RONO_2$ at both sites, consistent with our previous study at Tai O, a background site in southwestern Hong Kong (Lyu et al., 2015). In contrast, the reaction of RO+NO_2 made considerable contributions to CH_3ONO_2 (mean ± 95% confidence interval (C.I.): 2.7 ± 0.3 pptv or 41.9 ± 5.9% at TMS and 4.8 ± 1.0 pptv or 76.2 ± 15.7% at TW). In addition to higher CH_4 levels, the more abundant secondary CH_3ONO_2 at TW was likely because that NO_2 at TW (31.6 ± 3.1 ppbv) was significantly higher than that at TMS (8.7 ± 0.8 ppbv) ($p<0.05$). Indeed, following suggestions that RO+NO_2 could be an important pathway for CH_3ONO_2 formation in polluted environments (Flocke et al., 1998a; Simpson et al., 2006), Archibald et al. (2007) confirmed that this pathway becomes important at about 10 ppb of NO_2, and dominant at about 35 ppb, based on MCM simulations for European conditions. For C_2-C_3 $RONO_2$, although the measured parent hydrocarbons were less abundant at TMS than at TW, the simulated concentrations of RO_2 radicals were all remarkably higher under low NO_x conditions (as discussed below), leading to comparable (for $C_2H_5ONO_2$ and 2-$C_3H_7ONO_2$) or even higher (for 1-$C_3H_7ONO_2$) mixing ratios of $RONO_2$ at TMS. However, for C_4 $RONO_2$, the higher concentrations of its parent hydrocarbon *n*-C_4H_{10} (4131 ± 361 pptv) and NO (26.9 ± 2.9 ppbv) at TW resulted in higher levels of secondary

340 2-$C_4H_9ONO_2$ (17.6±2.4 pptv) because the concentration of 2-$C_4H_9O_2$ at TW was lower than
341 TMS by a factor of 4.2, compared to 6.7, 6.6 and 13.3 for $C_2H_5O_2$, 2-$C_3H_7O_2$ and 1-$C_3H_7O_2$,
342 respectively.

343 The difference in NO_x levels was considered to be the main cause of the anti-correlation between
344 the parent hydrocarbons and related RO_2 radicals. As O_3 formation is generally limited by VOCs
345 at both sites (Guo et al., 2013; Ling et al., 2014), the reaction chains of O_3 formation were
346 terminated by NO_x reacting with reactive radicals. Figure S4 shows that the simulated OH and
347 HO_2 levels were much lower at TW than at TMS. This is because the higher NO_x at TW
348 consumed more oxidative substances (*e.g.*, O_3) and radicals (OH and HO_2). Consequently,
349 reactions including the oxidation of parent hydrocarbons at TW were more suppressed, leading
350 to lower production efficiency of RO_2 radicals.

351 Table 2 Average mixing ratios of parent hydrocarbons, NO_x and secondary $RONO_2$ at TMS and
352 TW. Error bars represent 95% C.I.s.

	TMS	TW
CH_4 (ppbv)	1950±7	1970±7
C_2H_6 (pptv)	1848±76	2144±81 *
C_3H_8 (pptv)	1123±71	3343±331 *
***n*-C_4H_{10} (pptv)**	887±84	4131±361 *
NO (ppbv)	3.5±0.1	26.9±2.9 *
NO_2 (ppbv)	8.7±0.8	31.6±3.1 *
CH_3O_2 (molecules/cm^3)	$(3.1\pm0.4)\times10^7$ *	$(0.6\pm0.3)\times10^7$
$C_2H_5O_2$ (molecules/cm^3)	$(2.0\pm0.2)\times10^6$ *	$(0.3\pm0.1)\times10^6$
2-$C_3H_7O_2$ (molecules/cm^3)	$(4.6\pm0.5)\times10^5$ *	$(0.7\pm0.2)\times10^5$
1-$C_3H_7O_2$ (molecules/cm^3)	$(4.0\pm0.6)\times10^5$ *	$(0.3\pm0.1)\times10^5$
2-$C_4H_9O_2$ (molecules/cm^3)	$(7.1\pm0.8)\times10^5$ *	$(1.7\pm0.5)\times10^5$
Secondary CH_3ONO_2 (pptv)	2.7±0.3	4.8±1.0 *
Secondary $C_2H_5ONO_2$ (pptv)	4.0±0.4	3.6±0.7
Secondary 2-$C_3H_7ONO_2$ (pptv)	5.2±0.5	4.5±0.7

Secondary 1-$C_3H_7ONO_2$ (pptv)	1.1 ±0.1 *	0.7 ±0.1
Secondary 2-$C_4H_9ONO_2$ (pptv)	13.5 ±1.4	17.6 ±2.4 *

353 * Significant difference between the two sites (p<0.05). Bolded are species with observed values,
354 and the rest are simulated values.

355 Table 3 Relative contributions (%) of the RO_2+NO and RO+NO_2 pathways to $RONO_2$ at TMS
356 and TW. Error bars represent 95% C.I.s.

$RONO_2$	TMS		TW	
	RO_2+NO	RO+NO_2	RO_2+NO	RO+NO_2
CH_3ONO_2	58.1 ±6.8	41.9 ±5.9	23.8 ±4.8	76.2 ±15.7
$C_2H_5ONO_2$	99.0 ±13.4	1.0 ±0.2	95.8 ±24.2	4.2 ±1.2
2-$C_3H_7ONO_2$	99.6 ±12.7	0.4 ±0.1	98.9 ±19.4	1.1 ±0.2
1-$C_3H_7ONO_2$	99.5 ±12.4	0.5 ±0.1	98.1 ±17.8	1.9 ±0.4
2-$C_4H_9ONO_2$	99.9 ±14.1	0.10 ±0.02	99.7 ±18.4	0.3 ±0.1

357

358 To further investigate $RONO_2$ formation in different environments, a total of 225 scenarios were
359 designed for model simulations. Briefly, $RONO_2$ production was simulated with a matrix of total
360 VOCs (TVOCs) and NO_x ranging from 4-720 ppbv and 0.5-90 ppbv, respectively (TVOCs = 4, 8,
361 16, 32, 48, 64, 80, 160, 240, 320, 400, 480, 560, 640 and 720 ppbv; NO_x = 0.5, 1, 2, 4, 6, 8, 10,
362 20, 30, 40, 50, 60, 70, 80 and 90 ppbv). The rationale for concentration setting is to include the
363 observed TVOCs and NO_x in the middle of the sequence. Apart from their mixing ratios, the
364 composition of TVOCs and NO_x might also influence the production of $RONO_2$. Therefore, the
365 ratios between VOC species and NO and NO_2 (referred to as air pollutant profiles hereafter) at
366 TMS and TW were used to distribute VOCs species in TVOCs, and NO and NO_2 in NO_x. Figure
367 4 shows the isopleths of CH_3ONO_2 and $C_2H_5ONO_2$ production with the changes of TVOCs and
368 NO_x based on the air pollutant profiles at TMS (panels (a) and (b)) and TW (panels (c) and (d)).
369 The isopleth of $C_2H_5ONO_2$ production was selected as an example of C_2-C_4 $RONO_2$, which had
370 the same pattern variations in response to the changes of TVOCs and NO_x (see Figure S5). It is
371 noteworthy that both formation pathways of RO_2+NO and RO+NO_2 were considered for C_1-C_4
372 $RONO_2$. Based on Figure 4, the NO_x limited and VOC limited regimes in $RONO_2$ formation
373 were identified. Briefly, the points with the lowest TVOCs on each isopleth line (red dots in the

figure panels) were linked in a straight line (ridge line), and $RONO_2$ formation in the area below and above the line was limited by NO_x and VOCs, respectively. Please note, the red dots associated with NO_x of 90 ppbv (the largest scale for the y-axis) were excluded, because they might not be the turning points from a NO_x-limited to VOC-limited regime given that the isopleths for NO_x levels higher than 90 ppbv were not simulated. Consequently, the ridge lines ended in the middle of the plots. Linear regressions were carried out for these ridge linesand a TVOC/NO_x ratio of approximately 3.3/1 ppbv/ppbv (R^2=0.96) was obtained for the simulated production of C_2-C_4 $RONO_2$ based on the air pollutant profiles at TMS. In other words, when the ratio of TVOCs/NO_x was higher (lower) than 3.3/1 ppbv/ppbv, the C_2-C_4 $RONO_2$ formation was limited by NO_x (VOCs). However, this ratio was much higher based on the air pollutant profiles at TW (TVOCs/NO_x=8.1/1 ppbv/ppbv, R^2=0.99). This might be due to much lower levels of oxidative radicals (see Figure S4) and the more important role of NO_x in consuming oxidative radicals at this urban site (Ling et al., 2014), causing significant reduction of oxidative radicals even at a relatively high ratio of TVOCs/NO_x. Analysis of the relationship between $RONO_2$ production and the TVOC/NO_x ratio found that in the NO_x limited regime, increasing NO_x stimulated the production of $RONO_2$ (RO_2+NO→$RONO_2$). However, increasing NO_x led to a direct or indirect reduction of OH (OH+NO_2→HNO_3 and NO+O_3→NO_2+O_2) and subsequent reductions of HO_2, RO_2 and RO in the VOC limited regime. Conversely, an increase of TVOCs elevated the production of these radicals. Therefore, in the VOC limited regime, an increase of TVOCs (NO_x) resulted in an increase (decrease) of RO_2, subsequently stimulating (suppressing) $RONO_2$ formation.

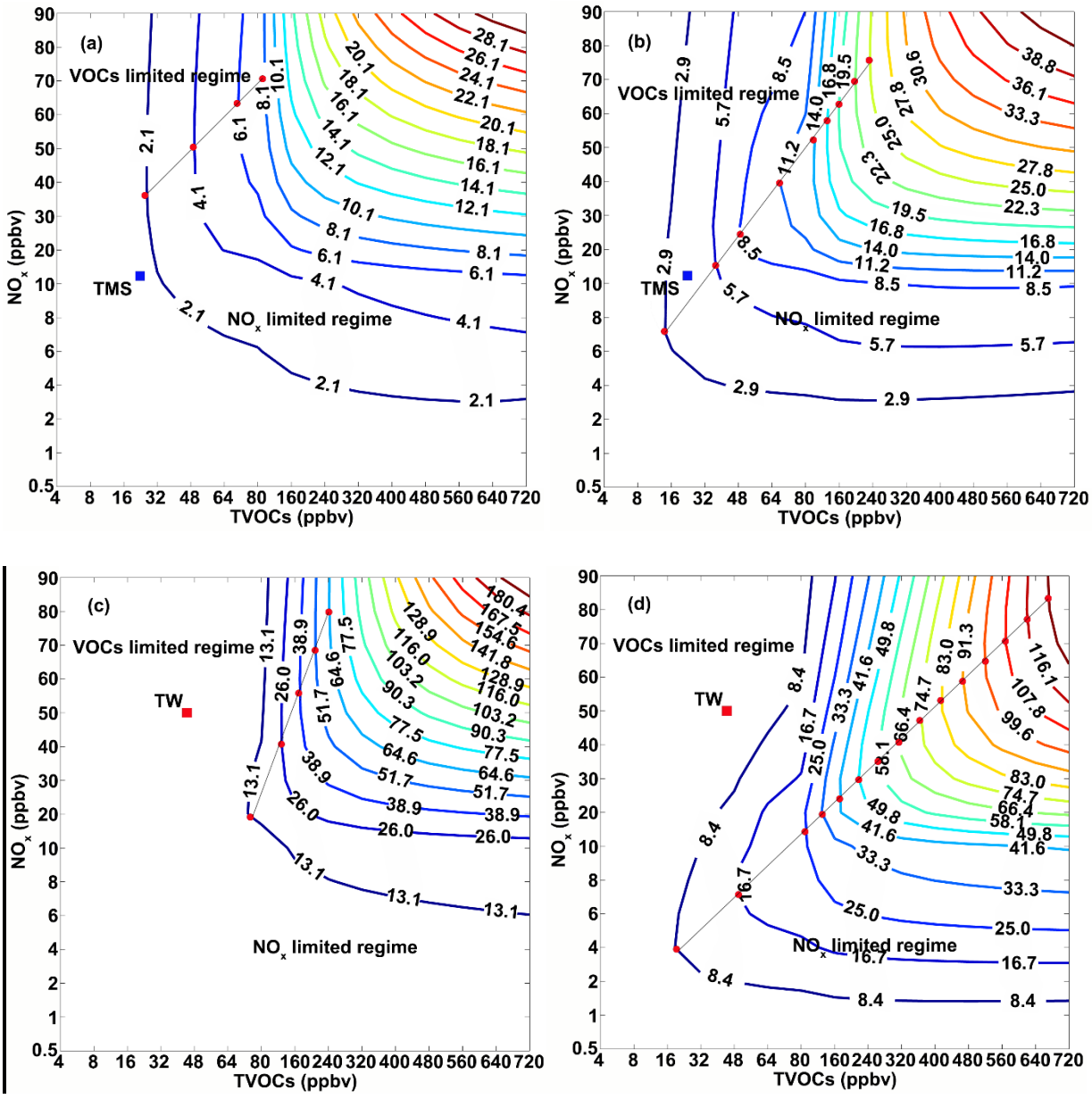

Figure 4 Isopleths of photochemical production of (a) CH_3ONO_2 and (b) $C_2H_5ONO_2$ (as an example of C_2-C_4 $RONO_2$) based on the air pollutant profiles at TMS; (c) CH_3ONO_2 and (d) $C_2H_5ONO_2$ (as an example of C_2-C_4 $RONO_2$) based on the air pollutant profiles at TW. The line with the red dots separates NO_x limited regime from VOCs limited regime. The blue and red blocks in the figure represent the average observed TVOCs, NO_x and simulated $RONO_2$ at TMS (blue) and TW (red), respectively.

Note that the threshold ratios of TVOC/NO_x turning to VOC-limited were lower for CH_3ONO_2 formation than for C_2-C_4 $RONO_2$ at both TMS and TW, which were around 1.8/1 ppbv/ppbv (R^2=0.98) and 3.0/1 ppbv/ppbv (R^2=0.99) based on the air pollutant profiles at TMS and TW, respectively. In contrast to C_2-C_4 $RONO_2$, which were mainly generated from RO_2 reacting with NO, CH_3ONO_2 had two pivotal formation pathways, *i.e.*, RO_2+NO and RO+NO_2 (Table 3). Figure 5 (a) and (b) show the respective isopleths of CH_3ONO_2 produced by the pathways of CH_3O_2+NO and CH_3O+NO_2 based on the air pollutant profiles at TMS (the isopleths at TW are presented in Figure 5 (c) and (d)). The CH_3ONO_2 generated by CH_3O_2+NO (panels (a) and (c)) followed the same patterns as C_2-C_4 $RONO_2$ (TVOCs/NO_x ratio of 3.3/1 and 8.1/1 ppbv/ppbv as the threshold between the VOC- and NO_x-limited regimes at TMS and TW, respectively). However, the ridge line separating the VOC- and NO_x-limited regimes was not determined at TMS for CH_3O+NO_2 (Figure 5 (b)), because the formation of CH_3ONO_2 was all limited by NO_x. Namely, based on the air pollutant profiles at TMS, the formation of CH_3ONO_2 from the CH_3O+NO_2 always increased with increasing NO_x, implying a continuous NO_x limited regime. Even based on the air pollutant profiles at TW, the simulation results indicated that NO_x did not facilitate CH_3ONO_2 formation until the ratio of TVOC/NO_x was lower than 2.9/1 ppbv/ppbv for the TVOC range of 4-160 ppbv. Moreover, for the scenarios with TVOCs $\geq$ 240 ppbv, CH_3ONO_2 generated from CH_3O + NO_2 continuously increased with increasing NO_x (continuous NO_x limited regime). The continuous stimulation effect of NO_x on CH_3ONO_2 formation at low ratios of TVOC/NO_x (high NO_x) was also identified by Archibald et al. (2007), which might be caused by the competitiveness of NO_2 associating with CH_3O relative to the oxidation of CH_3O ($CH_3O+O_2 \rightarrow HCHO+HO_2$) increasing under high NO_x.

In summary, Table 4 lists the ranges of TVOC/NO_x ratios corresponding to the NO_x limited and VOCs limited regimes in $RONO_2$ formation, which were simulated on the basis of the air pollutant profiles at TMS and TW. Please note: these values were the slopes derived from linear regressions. The uncertainty of model simulation was roughly estimated by root mean square of the accuracies of input parameters, which was ~13%.

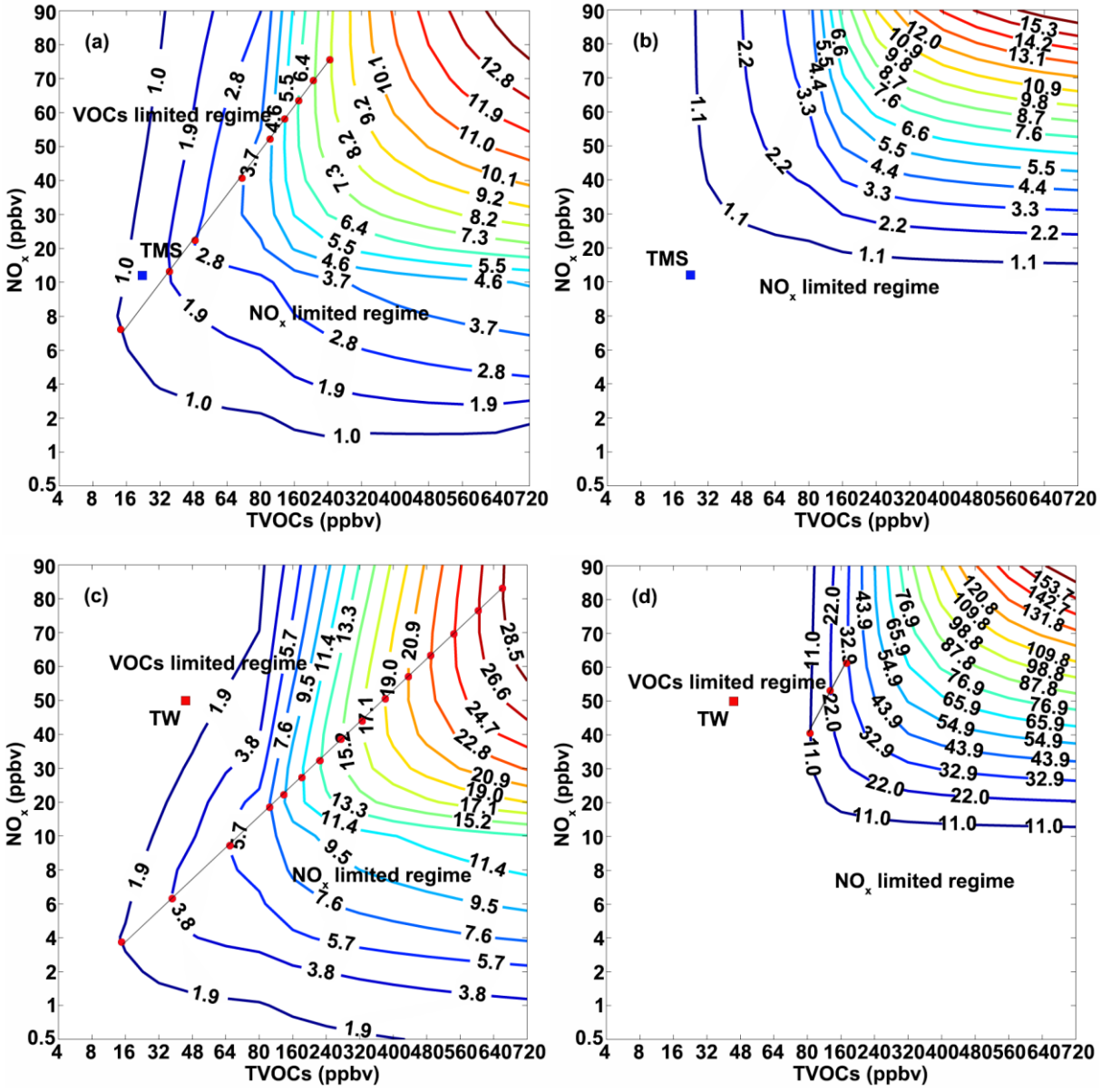

Figure 5 Isopleths of CH_3ONO_2 production from the pathway of (a) CH_3O_2+NO and (b) CH_3O+NO_2 based on the air pollutant profiles at TMS; (c) CH_3O_2+NO and (d) CH_3O+NO_2 based on the air pollutant profiles at TW.

Table 4 Ranges of TVOC/NO_x ratios corresponding to regimes controlling $RONO_2$ formation based on the air pollutant profiles at TMS and TW.

TVOCs/NO_x (ppbv/ppbv)	Profiles of air pollutants at TMS		Profiles of air pollutants at TW	
	NO_x limited	VOC limited	NO_x limited	VOCs limited
[a] CH_3ONO_2	>1.8/1	<1.8/1	>3.0/1	<3.0/1
[b] CH_3ONO_2	>3.3/1	<3.3/1	>8.1/1	<8.1/1
[c] CH_3ONO_2	All ratios	None	>2.9/1	<2.9/1
C_2-C_4 $RONO_2$	>3.3/1	<3.3/1	>8.1/1	<8.1/1

[a] Total CH_3ONO_2 produced by CH_3O_2+NO and CH_3O+NO_2; [b] CH_3ONO_2 produced by CH_3O_2+NO; [c] CH_3ONO_2 produced by CH_3O+NO_2.

3.3 Impacts on O_3 production

3.3.1 During $RONO_2$ formation

To investigate the impacts of $RONO_2$ formation on O_3 production, two categories of scenarios, *i.e.*, a base case and five constrained cases were tested in this study. Briefly, in the base case all reaction pathways were switched on in the model, while the formation pathways (RO_2+NO and RO+NO_2) of each individual $RONO_2$ were switched off in each corresponding constrained case. The five constrained cases corresponded to the five $RONO_2$. All other settings were identical between the base and constrained cases. The base case simulated the secondary production of $RONO_2$. The O_3 variations (ΔO_3) induced by $RONO_2$ formation were obtained by subtracting O_3 in the constrained cases from that in the base case, as were the variations of NO, NO_2, OH and HO_2. Figure 6 shows the relationship between ΔO_3 and secondary $RONO_2$ production at TMS and TW. Overall, as secondary $RONO_2$ production increased, O_3 levels decreased. The formation of CH_3ONO_2, $C_2H_5ONO_2$, 2-$C_3H_7ONO_2$, 1-$C_3H_7ONO_2$ and 2-$C_4H_9ONO_2$ caused an average O_3 reduction (mean $\pm$95% C.I.) of 9.7 $\pm$1.1, 14.7 $\pm$1.6, 18.4 $\pm$1.9, 6.9 $\pm$0.6 and 60.2 $\pm$6.8 pptv at TMS, and 10.5 $\pm$3.2, 7.1 $\pm$2.0, 8.3 $\pm$2.1, 2.0 $\pm$0.5 and 40.0 $\pm$9.8 pptv at TW, respectively. Furthermore, the O_3 reduction was linearly correlated with the production of secondary $RONO_2$ ($0.72 < R^2 < 0.95$ at TMS, $0.77 < R^2 < 0.84$ at TW) at TW for CH_3ONO_2, $C_2H_5ONO_2$, 2-$C_3H_7ONO_2$, 1-$C_3H_7ONO_2$ and 2-$C_4H_9ONO_2$, respectively. Notably, the O_3 reduction efficiencies

(ΔO_3/secondary $RONO_2$) were significantly lower at TW than at TMS (p<0.05), meaning that $RONO_2$ production caused less O_3 reduction at TW than at TMS. Since O_3 formation was generally limited by VOCs at TMS and TW (Ling et al., 2014), the variations of reactive radicals (RO, HO_2 and OH) during the $RONO_2$ formation were expected to be the main cause of O_3 reduction. This assumption was confirmed by the correlations of daily average O_3 reduction with daily average variations in simulated NO, NO_2, OH and HO_2 (hourly average values between 07:00 and 19:00), as shown in Figures S6-S7. The O_3 reduction correlated well with the reduction of OH (R^2= 0.83 and 0.71 at TMS and TW, respectively) and of HO_2 (R^2= 0.84 and 0.98 at TMS and TW, respectively), while poor correlations were found between O_3 reduction and the variation of NO or NO_2. As discussed earlier, OH and HO_2 at TW were much lower than at TMS (see Figure S4). Therefore, the lower O_3 reduction efficiencies at TW mainly resulted from the lower photochemical reactivity, which was unfavorable to the chain propagation of O_3 formation reactions.

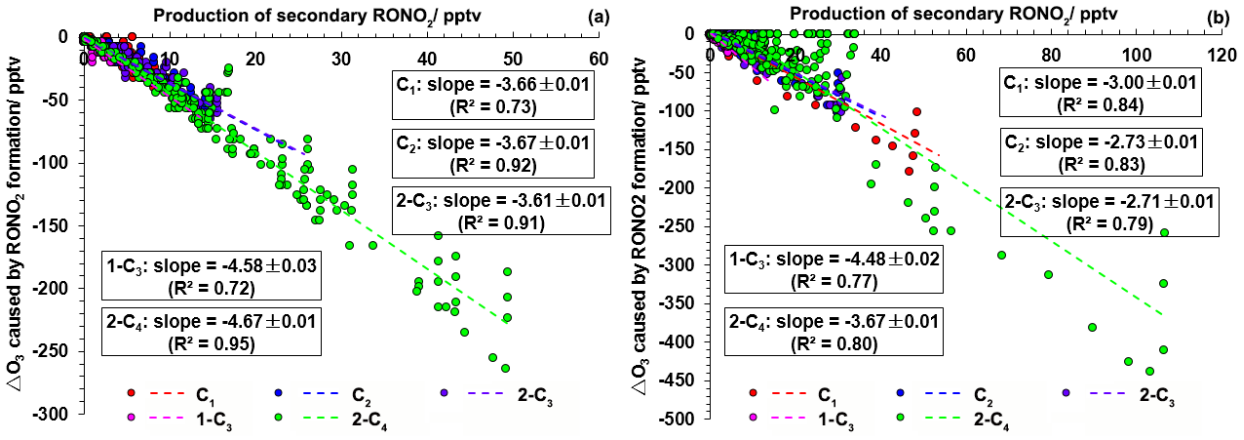

Figure 6 Relationship between O_3 reductions and the simulated secondary $RONO_2$ productions at (a) TMS and (b) TW.

3.3.2 During $RONO_2$ degradation

The oxidative radicals and NO_x stabilized within $RONO_2$ molecules can be released and fuel O_3 formation as the $RONO_2$ degrades. OH oxidation and photolysis are the main degradation pathways of $RONO_2$. Figure S8 shows the average simulated OH oxidation and photolysis rates for C_1-C_4 $RONO_2$ at TMS and TW. As expected based on the literature (*e.g.*, Clemitshaw et al., 1997), the photolysis of CH_3ONO_2 was stronger than its OH oxidation at both sites. As the

$RONO_2$ carbon number increases the importance of photolysis decreases (Atkinson et al., 1982b; Bertman et al., 1995; Clemitshaw et al., 1997). Here the OH oxidation rates were comparable to photolysis rates for $C_2H_5ONO_2$ and 2-$C_3H_7ONO_2$, and exceeded photolysis rates for 1-$C_3H_7ONO_2$ and 2-$C_4H_9ONO_2$ at TMS. However, at TW, the OH oxidation was still weaker than photolysis for $C_2H_5ONO_2$ and 2-$C_3H_7ONO_2$, and comparable to photolysis for 1-$C_3H_7ONO_2$ and 2-$C_4H_9ONO_2$. The weaker response of the OH oxidation rate to increasing carbon number at TW was ascribed to the lower OH concentration at TW ($1.1 \pm 0.2 \times 10^6$ molecules/cm^3) compared to TMS ($4.3 \pm 0.5 \times 10^6$ molecules/cm^3).

The impacts of $RONO_2$ degradation on O_3 production were studied with two simulation scenarios, *i.e.*, a base scenario with all the reaction pathways switched on and a constrained scenario in which OH oxidation and photolysis for all five C_1-C_4 $RONO_2$ were switched off. The differences of model output between the two scenarios reflected the impact of $RONO_2$ degradation. Note that this impact was studied in the form of total C_1-C_4 $RONO_2$ rather than individual species, because the highest resolution of the model output was 1×10^8 molecules/cm^3 (~4 pptv), and the small O_3 variation induced by individual $RONO_2$ could not be accurately simulated. During $RONO_2$ degradation NO_2 is released, which decomposes and generates NO and O, allowing O_3 to be formed from O_2 and O. On the other hand, the released NO_2 also reacts with OH, leading to the decreases of OH and HO_2, and reduced O_3 production. The RO released from $RONO_2$ degradation fuels O_3 formation. Therefore, the net impact of $RONO_2$ degradation on O_3 production involves the combined effect and relative strengths of NO_2 stimulating, NO_2 suppressing, and RO stimulating processes, which exist simultaneously in $RONO_2$ degradation.

Figure 7 shows the simulated daily average variations of O_3, NO, NO_2, OH and HO_2 induced by degradation of the C_1-C_4 $RONO_2$. The daily average O_3 variations ranged from -7.4 pptv to 2.3 pptv at TMS, but increased at TW throughout the sampling campaign (average increase of 2.9 ± 0.8 pptv). At TMS, the O_3 variation correlated well with the OH and HO_2 variations (R^2 of 0.86 and 0.85, respectively), but negatively with the variations of NO and NO_2 (R^2 of 0.89 and 0.76, respectively). This implied that O_3 formation at TMS was generally VOC-limited (NO_x-suppressed). When NO and NO_2 levels increased at TMS, O_3, OH and HO_2 decreased. This might be due to the consumption of OH by NO_2 and/or NO titration with O_3. Since NO increases resulted from the decomposition of NO_2, we defined this impact of $RONO_2$ degradation on O_3

production as NO_2 suppressing. In contrast, O_3 formation was enhanced by $RONO_2$ degradation on several days (October 29-31, November 02 and 21), when NO and NO_2 decreased while OH and HO_2 increased. Since NO_2 consumed oxidative radicals, while RO promoted their formation, the increases of OH and HO_2 in $RONO_2$ degradation indicated that the RO stimulating effect overrode the NO_2 suppressing effect in these cases, causing an O_3 increase. Thus, the impact of $RONO_2$ degradation on O_3 production manifested as RO stimulating. Consistently, O_3, OH and HO_2 all increased while NO decreased at TW, induced by $RONO_2$ degradation. Differing from NO_2 decrease in the scenarios of O_3 increase at TMS, NO_2 increased at TW, which might be caused by the lower concentration of OH at this urban site (so lower NO_2 consumption through $OH + NO_2 \rightarrow HNO_3$) and the higher O_3 increase (so higher NO_2 production through $O_3 + NO \rightarrow NO_2 + O_2$). Furthermore, the O_3 enhancement exhibited moderate to good correlations with the simulated increase of OH ($R^2 = 0.50$) and HO_2 ($R^2 = 0.81$), which were generated from the evolution of RO in the photochemical reaction chain. As such, the impact of $RONO_2$ degradation on O_3 production at TW was dominated by the effect of RO stimulating. In addition, the ratio of $TVOC/NO_x$ in cases of O_3 increase at TMS (average: 2.1/1 ppbv/ppbv) was higher than in cases of O_3 decrease (average ratio: 1.6/1 ppbv/ppbv). The lower ratio of $TVOC/NO_x$ means that O_3 formation was more limited by VOCs, which enabled the added RO to more efficiently stimulate O_3 formation and resulted in the increase of O_3. Coincidently, the low ratio of $TVOC/NO_x$ (0.9/1 ppbv/ppbv) at TW also caused O_3 increase during $RONO_2$ degradation.

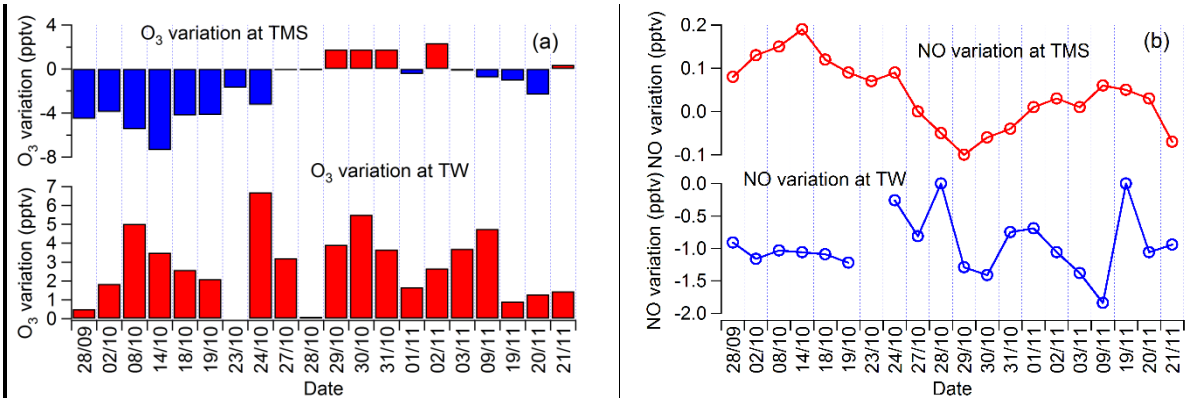

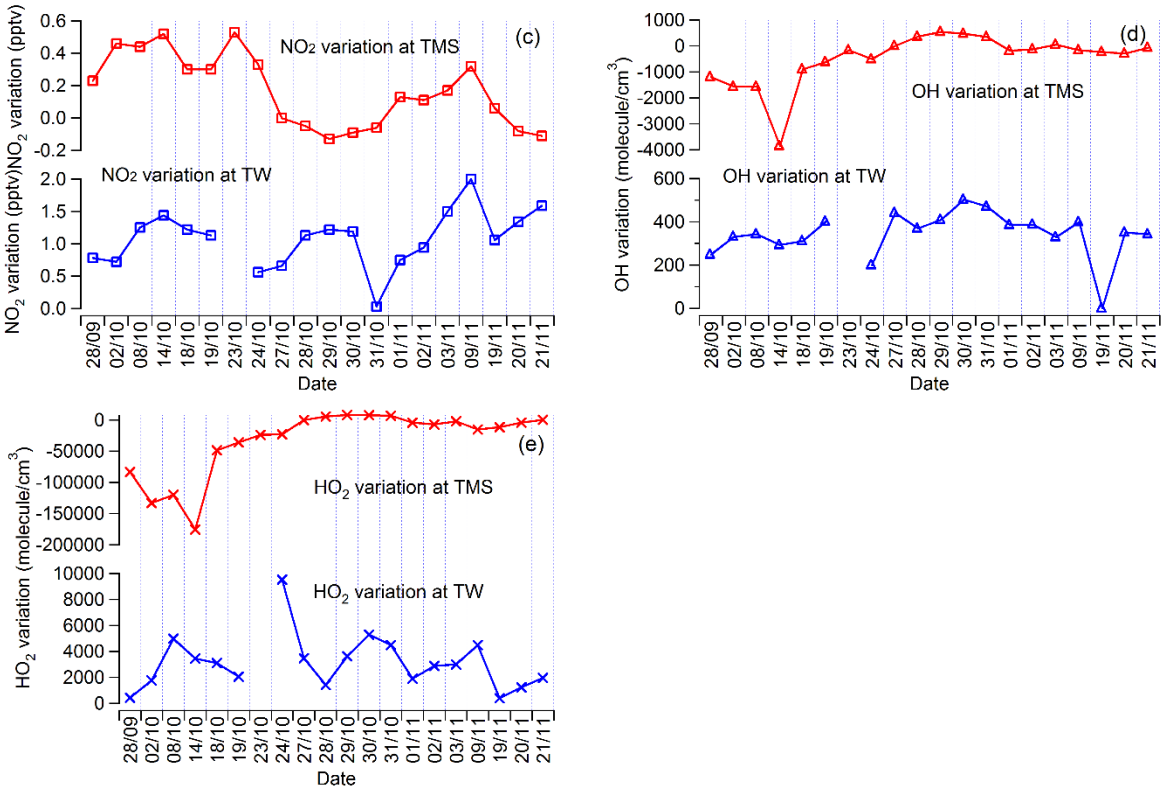

Figure 7 Simulated variations of (a) O_3, (b) NO, (c) NO_2, (d) OH and (e) HO_2 at TMS and TW induced by C_1-C_4 $RONO_2$ degradation.

To extend the impact of $RONO_2$ degradation on O_3 production to different environments, O_3 production in a total of 225 base scenarios and 225 constrained scenarios were simulated. The scenarios were constructed with 15 gradients of TVOCs (TVOCs = 4, 8, 16, 32, 48, 64, 80, 160, 240, 320, 400, 480, 560, 640 and 720 ppbv) and 15 gradients of NO_x (NO_x = 0.5, 1, 2, 4, 6, 8, 10, 20, 30, 40, 50, 60, 70, 80 and 90 ppbv). Similar to the simulations of $RONO_2$ formation, these simulations were based on the air pollutant profiles at TMS and TW, respectively. The degradation reactions of C_1-C_4 $RONO_2$ were switched off in all the constrained scenarios. Figure 8 and Figure 9 show the average differences of O_3, NO, NO_2, OH, HO_2 and total C_1-C_4 $RONO_2$ between each base scenario and its corresponding constrained scenario, based on the air pollutant profiles at TMS and TW, respectively. The negative values to the right of the y-axis in panel (f) indicates the degradation amounts of total C_1-C_4 $RONO_2$ (the difference of simulated $RONO_2$ between the base and constrained scenarios), and panels (a)-(e) reflect the impact of the $RONO_2$

553 degradation on the production of these compounds or radicals. To help understand the variations
554 of these species or radicals, the NO_x-limited and VOC-limited regimes in O_3 formation at TMS
555 and TW are shown in Figure S9. Notably, the variation patterns of O_3 with the changes of
556 TVOCs and NO_x were highly consistent with those of C_2-C_4 $RONO_2$. Namely, 3.3/1 and 8.1/1
557 ppbv/ppbv were the threshold TVOC/NO_x ratios separating the NO_x and VOC limited regimes.
558 This is reasonable because C_2-C_4 $RONO_2$ and O_3 share the same formation pathways.

559 According to Figure 8 and Figure 9, with the degradation of C_1-C_4 $RONO_2$, O_3 generally
560 increased in the NO_x limited regime, regardless of the site. The increase of O_3 was always
561 accompanied by increased NO and NO_2 (panels (b) and (c)). However, the oxidative radicals
562 (OH and HO_2) could either increase or decrease with $RONO_2$ degradation in the NO_x limited
563 regime. For the convenience of discussion, the areas with OH or HO_2 increases (decreases) were
564 defined as "R1" ("R2") in panels (d) and (e). The OH and HO_2 increases might be caused by the
565 increase of O_3 following by the photolysis. The added RO from $RONO_2$ degradation also
566 facilitated the production of these oxidative radicals. However, in areas "R2" where more
567 $RONO_2$ was degraded and more NO_2 was released (see panels (c) and (f)), OH and HO_2
568 decreased, possibly from the higher consumption of OH by NO_2 that was released from $RONO_2$
569 degradation and/or consumption of OH by $RONO_2$ itself ($RONO_2+OH \rightarrow RO+NO_2+products$).
570 Since O_3 formation was limited by NO_x in this regime, the O_3 increase was most likely related to
571 stimulation of O_3 formation by NO_2 released from $RONO_2$ degradation. Note that this NO_2
572 stimulating effect on O_3 production was not observed at TMS and TW, where O_3 formation was
573 generally VOC limited. In contrast, O_3 either decreased or increased with $RONO_2$ degradation in
574 the VOC limited regime.

575 In the areas close to the NO_x limited regime (defined as area "R3"), O_3 generally decreased.
576 Consistently, both OH and HO_2 decreased in this area due to $RONO_2$ degradation, while NO and
577 NO_2 increased. It is widely known that VOCs and NO_x favor and inhibit O_3 formation in the
578 VOC limited regime, respectively. Since $RONO_2$ degradation released RO and NO_2, the decrease
579 of O_3 implied that the effect of NO_2 suppression overrode the effect of RO stimulation on O_3
580 formation. In other words, the net impact of $RONO_2$ degradation on O_3 production was NO_2
581 suppression in this area "R3". However, $RONO_2$ degradation led to a slight O_3 increase in
582 another area of the VOC limited regimes (defined as area "R4"), where OH and HO_2 also

583 increased. The average variations of O_3, NO, NO_2, OH and HO_2 are annotated in area "R4" for
584 panels (a)-(e) in Figures 8 and 9. Note that these variations were minor and difficult to
585 distinguish; the O_3 variations in this area are separately shown in Figure S10. In view of the
586 VOC limited regime controlling O_3 formation and the synchronous increases of O_3, OH and HO_2,
587 the O_3 increase induced by $RONO_2$ degradation was attributable to the addition of RO and its
588 stimulating effect on O_3 formation. Namely, RO stimulation overrode NO_2 suppression in area
589 "R4". Since area "R4" had lower TVOCs and higher NO_x than "R3", the change from NO_2
590 suppression in "R3" to RO stimulation in "R4" might be driven by the lower ratio of TVOC/NO_x,
591 as discussed earlier.

592 Moreover, in accordance with the simulations at TMS and TW (see Figure 7), the O_3 variations
593 induced by the degradation of C_1-C_4 $RONO_2$ with changing TVOCs and NO_x (panel (a)) also
594 revealed that O_3 production decreased (at a relatively higher ratio of TVOC/NO_x, point "TMS1"
595 in Figure 8) or increased (at a relatively lower ratio of TVOC/NO_x, point "TMS2" in Figure 8) at
596 TMS, and was consistently elevated at TW (point "TW" in Figure 9).

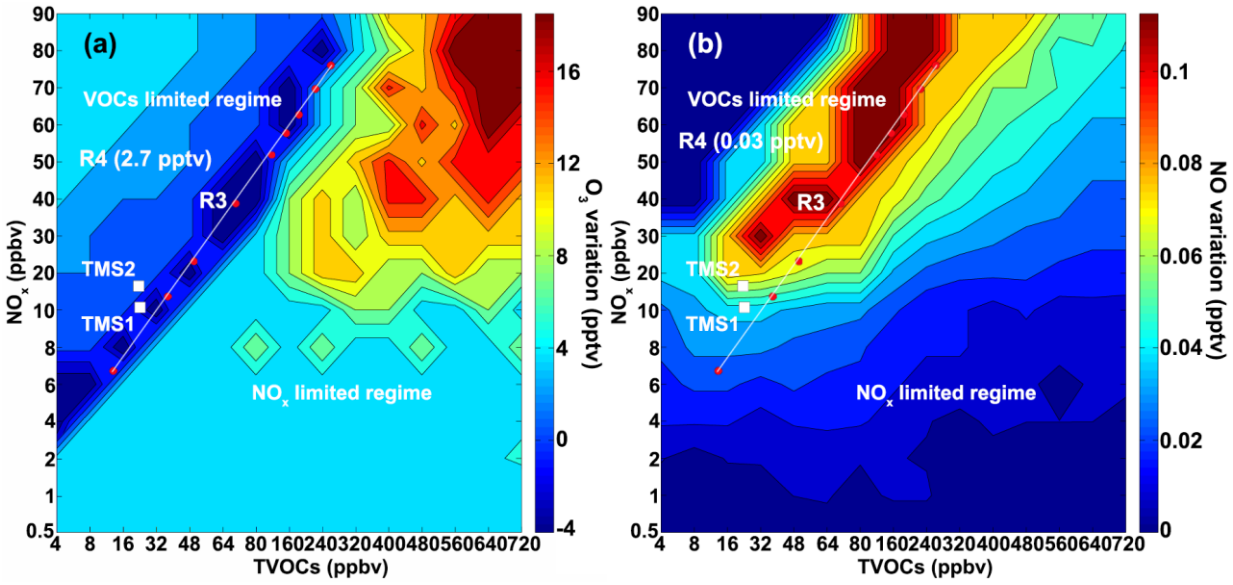

597

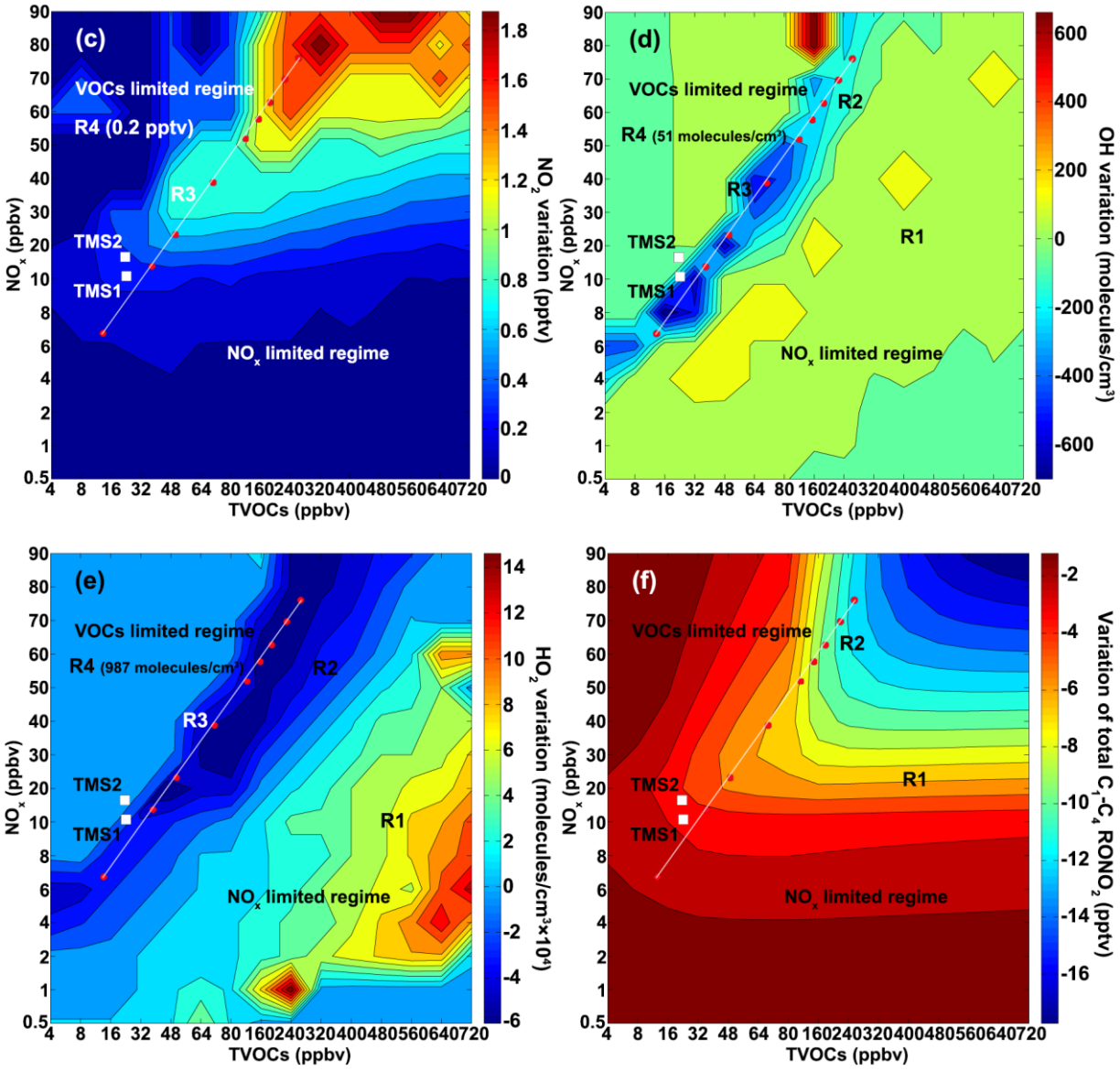

Figure 8 Variations of (a) O_3 (b) NO (c) NO_2 (d) OH (e) HO_2 and (f) total C_1-C_4 $RONO_2$ induced by the degradation of C_1-C_4 $RONO_2$ following changes of TVOCs and NO_x, simulated based on air pollutant profiles at TMS. The white squares "TMS1" and "TMS2" show the average simulated variations based on the measured TVOCs and NO_x at TMS in the cases of O_3 decrease and increase, respectively. Area "R1" (or "R2") shows the increases (or decreases) of OH/HO_2 in the NO_x limited regime. "R3" (or "R4") are areas with O_3 decrease (or increase) in the VOC limited regime. Numbers in the brackets of "R4" present the average variation of each species.

608

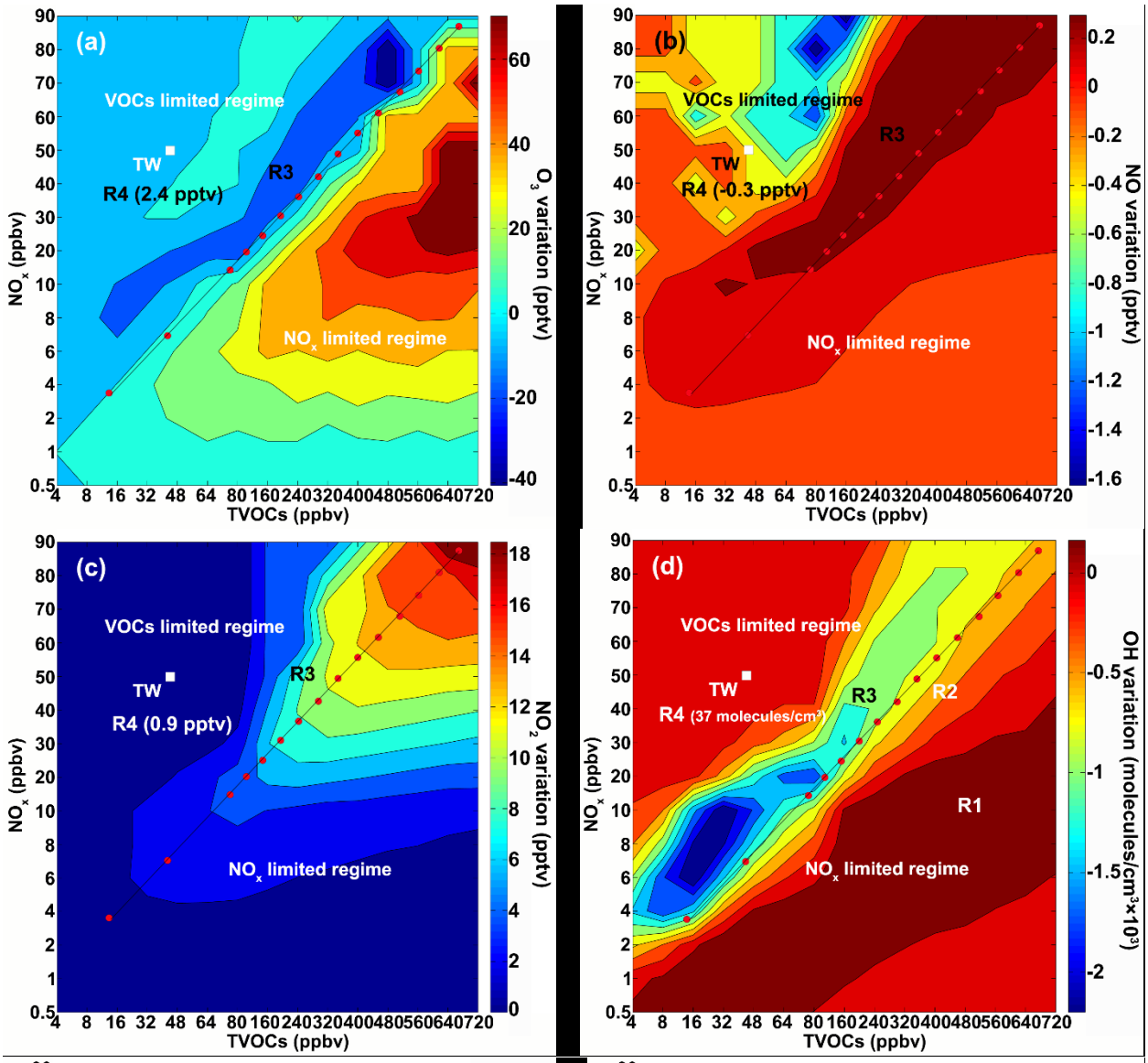
(a)
VOCs limited regime
TW
R4 (2.4 pptv)
R3
NOx limited regime
NOx (ppbv)
TVOCs (ppbv)
O3 variation (pptv)
(b)
VOCs limited regime
R3
TW
R4 (-0.3 pptv)
NOx limited regime
NO variation (pptv)
(c)
VOCs limited regime
TW
R4 (0.9 pptv)
R3
NOx limited regime
NO2 variation (pptv)
(d)
VOCs limited regime
TW
R4 (37 molecules/cm³)
R3
R2
R1
NOx limited regime
OH variation (molecules/cm³×10³)
(e)
VOCs limited regime
TW
R4 (926 molecules/cm³)
R3
R2
R1
NOx limited regime
HO2 (molecules/cm³×10⁵)
(f)
VOCs limited regime
TW
R2
R1
NOx limited regime
Variation of total C1-C4 RONO2 (pptv)

609

610

Figure 9 Variations of (a) O_3 (b) NO (c) NO_2 (d) OH (e) HO_2 and (f) total C_1-C_4 $RONO_2$ induced by the degradation of C_1-C_4 $RONO_2$ following changes of TVOCs and NO_x, simulated based on air pollutant profiles at TW. The white square "TW" shows the average simulated variations based on the measured TVOCs and NO_x at TW. Area "R1" (or "R2") shows the increases (or decreases) of OH/HO_2 in the NO_x limited regime. "R3" (or "R4") are areas with O_3 decrease (or increase) in the VOC limited regime. Numbers in the brackets of "R4" present the average variation of each species.

4 Conclusions

A PBM-MCM model was developed to simulate gas-phase $RONO_2$ measured at an urban and a mountainous site in Hong Kong. The magnitudes and variations of the observed C_1-C_4 $RONO_2$ at both sites were well reproduced by the model. The modeling results indicated that $RONO_2$ formation depended upon not only the abundances of precursors but also the photochemical reactivity, which was closely related to the levels of VOCs and NO_x. Although the precursors of $RONO_2$ at the mountainous site were less abundant than at the urban site, the higher photochemical reactivity led to higher production of RO_2 radicals, resulting in comparable or even higher $RONO_2$. The regimes in which the formation of C_2-C_4 $RONO_2$ was NO_x-limited and VOC-limited were identified namely when the ratio of $TVOC/NO_x$ was higher and lower than 3.3/1 ppbv/ppbv, respectively, based on the air pollutant profiles at mountainous site. Since the NO_x concentration was higher at the urban site, the formation of C_2-C_4 $RONO_2$ was limited by NO_x when the ratio of $TVOC/NO_x$ was higher than 8.1/1. However, these simulated thresholds decreased to 1.8/1 and 3.0/1 ppbv/ppbv for the formation of CH_3ONO_2 at the mountainous and urban site, respectively. This was mainly because CH_3ONO_2 produced from $CH_3O + NO_2$ continued to increase with increasing NO_x when the ratios of $TVOC/NO_x$ were relatively low (high NO_x). Since O_3 formation was generally VOC limited at both sites, and $RONO_2$ formation initially stabilized RO radicals in $RONO_2$ molecules, O_3 production was reduced by $RONO_2$ formation. On the other hand, the mechanisms of $RONO_2$ degradation influencing O_3 production included NO_2 stimulating, NO_2 suppressing, and RO stimulating processes. At the mountainous site, the impact of $RONO_2$ degradation on O_3 production was dominated by NO_2 suppression under the condition of relatively high ratios of $TVOC/NO_x$, leading to the decrease of O_3, while

RO stimulation occurred at relatively low ratios of TVOC/NO_x, resulting in the increase of O_3. However, the O_3 production always increased due to RO stimulation at the urban site.

Acknowledgements: This study was supported by the Research Grants Council of the Hong Kong Special Administrative Region via grants PolyU5154/13E, PolyU152052/14E, CRF/C5004-15E and CRF/C5022-14G, and the Hong Kong Polytechnic University PhD scholarships (project #RTUP). This study is partly supported by the Hong Kong PolyU internal grant (G-YBHT, 1-BBW4 and 4-ZZFW) and the National Natural Science Foundation of China (No. 41275122). The data are accessible at https://drive.google.com/file/d/0B0r5QxfKPoyUYTNyNUctcWNaeTg/view?usp=sharing.

References:

Archibald, A.T., Khan, M.A.H., Watson, L.A., Clemitshaw, K.C., Utembe, S.R., Jenkin, M.E., and Shallcross, D.E., 2007. Comment on 'Long-term atmospheric measurements of C_1-C_5 alkyl nitrates in the Pearl River Delta region of southeast China'by Simpson et al. Atmos. Environ. 41(34), 7369-7370.

Arey, J., Aschmann, S.M., Kwok, E.S., and Atkinson, R., 2001. Alkyl nitrate, hydroxyalkyl nitrate, and hydroxycarbonyl formation from the NO_x-air photooxidations of C_5-C_8 n-alkanes. J. Phys. Chem. A, 105(6), 1020-1027.

Aruffo, E., Di Carlo, P., Dari-Salisburgo, C., Biancofiore, F., Giammaria, F., Busilacchio, M., Lee, J., Moller, S., Hopkins, J., Punjabi, S., Bauguitte, S., O'Sullivan, D., Percival, C., Le Breton, M., Muller, J., Jones, R., Forster, G., Reeves, C., Heard, D., Walker, H., Ingham, T., Vaughan, S., and Stone, D., 2014. Aircraft observations of the lower troposphere above a megacity: Alkyl nitrate and ozone chemistry. Atmos. Environ. 94, 479-488.

Atkinson, R., 1990. Gas-phase tropospheric chemistry of organic compounds: a review. Atmos. Environ. Part A. General Topics, 24(1), 1-41.

Atkinson, R., Aschmann, S.M., Carter, W.P., and Winer, A.M., 1982b. Kinetics of the gas-phase reactions of OH radicals with alkyl nitrates at 299±2 K. Int. J. Chem. Kinet. 14(8), 919-926.

Atkinson, R., Aschmann, S.M., Carter, W.P., Winer, A.M., and Pitts Jr, J.N., 1982a. Alkyl nitrate formation from the nitrogen oxide (NO_x)-air photooxidations of C_2-C_8 n-alkanes. J. Phys. Chem. 86(23), 4563-4569.

Atkinson, R., Aschmann, S.M., and Winer, A.M., 1987. Alkyl nitrate formation from the reaction of a series of branched RO_2 radicals with NO as a function of temperature and pressure. J. Atmos. Chem. 5(1), 91-102.

Atlas, E., Pollock, W., Greenberg, J., Heidt, L., and Thompson, A.M., 1993. Alkyl nitrates, nonmethane hydrocarbons, and halocarbon gases over the equatorial Pacific Ocean during SAGA 3. J. Geophys. Res.: Atmos. 98(D9), 16933-16947.

675 Becker, K.H., and Wirtz, K., 1989. Gas phase reactions of alkyl nitrates with hydroxyl radicals
676 under tropospheric conditions in comparison with photolysis. J. Atmos. Chem. 9(4), 419-433.

677 Bertman, S.B., Roberts, J.M., Parrish, D.D., Buhr, M.P., Goldan, P.D., Kuster, W.C., Fehsenfeld,
678 F.C., Montzka, S.A., and Westberg, H., 1995. Evolution of alkyl nitrates with air mass age. J.
679 Geophys. Res.: Atmos. 100(D11), 22805-22813.

680 Buhr, M.P., Parrish, D.D., Norton, R.B., Fehsenfeld, F.C., Sievers, R.E., and Roberts, J.M., 1990.
681 Contribution of organic nitrates to the total reactive nitrogen budget at a rural eastern US site.
682 J. Geophys. Res.: Atmos. 95(D7), 9809-9816.

683 Carter, W.P., and Atkinson, R., 1985. Atmospheric chemistry of alkanes. J. Atmos. Chem. 3(3),
684 377-405.

685 Carter, W.P., and Atkinson, R., 1989. Alkyl nitrate formation from the atmospheric
686 photoxidation of alkanes; a revised estimation method. J. Atmos. Chem. 8(2), 165-173.

687 Chameides, W.L., Lindsay, R.W., Richardson, J., and Kiang, C.S., 1988. The role of biogenic
688 hydrocarbons in urban photochemical smog: Atlanta as a case study. Science (Washington),
689 241(4872), 1473-1475.

690 Chen, X., Hulbert, D., and Shepson, P.B., 1998. Measurement of the organic nitrate yield from
691 OH reaction with isoprene. J. Geophys. Res. 103(D19), 25-563.

692 Cheung, K., Guo, H., Ou, J.M., Simpson, I.J., Barletta, B., Meinardi, S., and Blake, D.R., 2014.
693 Diurnal profiles of isoprene, methacrolein and methyl vinyl ketone at an urban site in Hong
694 Kong. Atmos. Environ. 84, 323-331.

695 Clemitshaw, K.C., Williams, J., Rattigan, O.V., Shallcross, D.E., Law, K.S., and Cox, R.A.,
696 1997. Gas-phase ultraviolet absorption cross-sections and atmospheric lifetimes of several
697 C2-C5 alkyl nitrates. J. Photoch. Photobio. A: Chem. 102(2), 117-126.

698 Darnall, K.R., Carter, W.P., Winer, A.M., Lloyd, A.C., and Pitts Jr, J.N., 1976. Importance of
699 RO_2+nitric oxide in alkyl nitrate formation from C_4-C_6 alkane photooxidations under
700 simulated atmospheric conditions. J. Phys. Chem. 80(17), 1948-1950.

701 Day, D.A., Dillon, M.B., Wooldridge, P.J., Thornton, J.A., Rosen, R.S., Wood, E.C., and Cohen,
702 R.C., 2003. On alkyl nitrates, O_3, and the "missing NO_y". J. Geophys. Res.: Atmos. 108(D16).

703 Dimitriades, B. (1977, January). An alternative to the appendix-J method for calculating oxidant-
704 and NO_2-related control requirements. In International Conference on Photochemical Oxidant
705 Pollutant and Its Control: Proceedings (Vol. 2).

706 Farmer, D.K., Perring, A.E., Wooldridge, P.J., Blake, D.R., Baker, A., Meinardi, S., Huey, L.G.,
707 Tanner, D., Vargas, O., and Cohen, R. C., 2011. Impact of organic nitrates on urban ozone
708 production. Atmos. Chem. Phys. 11(9), 4085-4094.

709 Flocke, F., Atlas, E., Madronich, S., Schauffler, S.M., Aikin, K., Margitan, J.J., and Bui, T.P.,
710 1998b. Observations of methyl nitrate in the lower stratosphere during STRAT: Implications
711 for its gas phase production mechanisms. Geophys. Res. Lett. 25(11), 1891-1894.

Flocke, F., Volz-Thomas, A., Buers, H.J., Patz, W., Garthe, H.J., and Kley, D., 1998a. Long-term measurements of alkyl nitrates in southern Germany: 1. General behavior and seasonal and diurnal variation. J. Geophys. Res.: Atmos. 103(D5), 5729-5746.

Giacopelli, P., Ford, K., Espada, C., and Shepson, P.B., 2005. Comparison of the measured and simulated isoprene nitrate distributions above a forest canopy. J. Geophys. Res.: Atmos. 110(D1).

Guo, H., Jiang, F., Cheng, H.R., Simpson, I.J., Wang, X.M., Ding, A.J., Wang, T.J., Saunders, S.M., Wang, T., Lam, S.H.M., Blake, D.R., Zhang, Y.L., and Xie, M., 2009. Concurrent observations of air pollutants at two sites in the Pearl River Delta and the implication of regional transport. Atmos. Chem. Phys., 9(19), 7343-7360.

Guo, H., Ling, Z.H., Cheung, K., Jiang, F., Wang, D.W., Simpson, I.J., Barletta, B., Meinardi, S., Wang, T.J., Wang, X.M., Saunders, S. M., and Blake, D.R., 2013. Characterization of photochemical pollution at different elevations in mountainous areas in Hong Kong. Atmos. Chem. Phys. 13(8), 3881-3898.

Hurley, P.J., Blockley, A., and Rayner, K., 2001. Verification of a prognostic meteorological and air pollution model for year-long predictions in the Kwinana industrial region of Western Australia. Atmos. Environ. 35, 1871-1880.

Khan, M.A.H., Cooke, M.C., Utembe, S.R., Morris, W.C., Archibald, A.T., Derwent, R.G., Jenkin, M.E., Orr-Ewing, A.J., Higgins, C.M., Percival, C.J., Leather, K.E., and Shallcross, D.E., 2015. Global modeling of the C_1-C_3 alkyl nitrates using STOCHEM-CRI. Atmos. Environ. 123, 256-267.

Lam, K.S., Wang, T.J., Wu, C.L., and Li, Y.S., 2005. Study on an ozone episode in hot season in Hong Kong and transboundary air pollution over Pearl River Delta region of China, Atmos. Environ. 39, 1967-1977.

Lam, S.H.M., Saunders, S.M., Guo, H., Ling, Z.H., Jiang, F., Wang, X.M., and Wang, T.J., 2013. Modelling VOC source impacts on high ozone episode days observed at a mountain summit in Hong Kong under the influence of mountain-valley breezes. Atmos. Environ. 81, 166-176.

Lewis, A.C., Carslaw, N., Marriott, P.J., Kinghorn, R.M., Morrison, P., Lee, A.L., Bartle, K.D. and Pilling, M.J., 2000. A larger pool of ozone-forming carbon compounds in urban atmospheres. Nature, 405(6788), 778-781.

Lightfoot, P.D., Cox, R.A., Crowley, J.N., Destriau, M., Hayman, G.D., Jenkin, M.E., Moortgat, G.K., and Zabel, F., 1992. Organic peroxy radicals: kinetics, spectroscopy and tropospheric chemistry. Atmos. Environ. Part A. General Topics, 26(10), 1805-1961.

Ling, Z.H., Guo, H., Lam, S.H.M., Saunders, S.M., and Wang, T., 2014. Atmospheric photochemical reactivity and ozone production at two sites in Hong Kong: Application of a Master Chemical Mechanism-photochemical box model. J. Geophys. Res.: Atmos. 119(17), 10567-10582.

Ling, Z.H., Guo, H., Simpson, I.J., Saunders, S.M., Lam, S.H.M., Lyu, X.P., and Blake, D.R., 2016. New insight into the spatiotemporal variability and source apportionments of C_1-C_4 alkyl nitrates in Hong Kong. Atmos. Chem. Phys. 16, 8141-8156.

Lyu, X.P., Ling, Z.H., Guo, H., Saunders, S.M., Lam, S.H.M., Wang, N., Wang, Y., Liu, M., Wang, T., 2015. Re-examination of C_1-C_5 alkyl nitrates in Hong Kong using an observation-based model. Atmos. Environ. 120, 28-37.

Madronich, S., and Flocke, S., 1997. Theoretical estimation of biologically effective UV radiation at the Earth's surface. In: Zerefos, C. (Ed.), Solar Ultraviolet Radiation-Modeling, Measurements and Effects, NATO ASI Series, vol. I52. Springer-Verlag, Berlin.

Moore, R.M., and Blough, N.V., 2002. A marine source of methyl nitrate. Geophys. Res. Lett. 29(15).

Muthuramu, K., Shepson, P.B., Bottenheim, J.W., Jobson, B.T., Niki, H., and Anlauf, K.G., 1994. Relationships between organic nitrates and surface ozone destruction during Polar Sunrise Experiment 1992. J. Geophys. Res.: Atmos. 99(D12), 25369-25378.

Ou, J., Yuan, Z., Zheng, J., Huang, Z., Shao, M., Li, Z., Huang, X., Guo, H., and Louie, P., 2016. Ambient ozone control in a photochemically active region: short-term despiking or long-term attainment? Environ. Sci. Technol. 50(11), 5720-5728.

Perring, A.E., Bertram, T.H., Farmer, D.K., Wooldridge, P.J., Dibb, J., Blake, N.J., Blake, D.R., Singh, H.B., Fuelberg, H., Diskin, G., and Sachse, G., 2010. The production and persistence of $\Sigma RONO_2$ in the Mexico City plume. Atmos. Chem. Phys. 10(15), 7215-7229.

Perring, A.E., Pusede, S.E., and Cohen, R.C., 2013. An observational perspective on the atmospheric impacts of alkyl and multifunctional nitrates on ozone and secondary organic aerosol. Chem. Rev. 113(8), 5848-5870.

Roberts, J.M., and Fajer, R.W., 1989. UV absorption cross sections of organic nitrates of potential atmospheric importance and estimation of atmospheric lifetimes. Environ. Sci. Technol. 23(8), 945-951.

Rosen, R.S., Wood, E.C., Wooldridge, P.J., Thornton, J.A., Day, D.A., Kuster, W., Williams, E.J., Jobson, B.T., and Cohen, R.C., 2004. Observations of total alkyl nitrates during Texas Air Quality Study 2000: Implications for O_3 and alkyl nitrate photochemistry. J. Geophys. Res.: Atmos. (1984–2012), 109(D7).

Saunders, S.M., Jenkin, M.E., Derwent, R.G., and Pilling, M.J., 2003. Protocol for the development of the Master Chemical Mechanism, MCM v3 (Part A): tropospheric degradation of non-aromatic volatile organic compounds. Atmos. Chem. Phys. 3(1), 161-180.

Shao, M., Zhang, Y., Zeng, L., Tang, X., Zhang, J., Zhong, L., and Wang, B., 2009. Ground-level ozone in the Pearl River Delta and the roles of VOC and NO_x in its production. J. Environ. Manage. 90(1), 512-518.

Sillman, S., and He, D., 2002. Some theoretical results concerning O_3-NO_x-VOC chemistry and NO_x-VOC indicators. J. Geophys. Res.: Atmos. 107(D22).

Simpson, I.J., Meinardi, S., Blake, D.R., Blake, N.J., Rowland, F.S., Atlas, E., and Flocke, F., 2002. A biomass burning source of C_1-C_4 alkyl nitrates. Geophys. Res. Lett. 29(24).

Simpson, I.J., Wang, T., Guo, H., Kwok, Y.H., Flocke, F., Atlas, E., Meinardi, S., Sherwood Rowland, F., and Blake, D. R., 2006. Long-term atmospheric measurements of C_1-C_5 alkyl nitrates in the Pearl River Delta region of southeast China. Atmos. Environ. 40(9), 1619-1632.

Simpson, I.J., Akagi, S.K., Barletta, B., Blake, N.J., Choi, Y., Diskin, G.S., Fried, A., Fuelberg, H.E., Meinardi, S., Rowland, F.S., Vay, S.A., Weinheimer, A.J., Wennberg, P.O., Wiebring, P., Wisthaler, A., Yang, M., Yokelson, R.J., Blake, D.R., 2011. Boreal forest fire emissions in fresh Canadian smoke plumes: C_1-C_{10} volatile organic compounds (VOCs), CO_2, CO, NO_2, NO, HCN and CH_3CN. *Atmos. Chem. Phy*s., 11, 6445–6463.

Thornton, J.A., Wooldridge, P.J., Cohen, R.C., Martinez, M., Harder, H., Brune, W.H., Williams, E.J., Roberts, J.M., Fehsenfeld, F.C., Hall, S.R., Shetter, R.E., Wert, B.P., and Fried, A., 2002. Ozone production rates as a function of NO_x abundances and HO_x production rates in the Nashville urban plume. J. Geophys. Res.: Atmos. 107(D12).

Wang, N., Guo, H., Jiang, F., Ling, Z.H., and Wang, T., 2015. Simulation of ozone formation at different elevations in mountainous area of Hong Kong using WRF-CMAQ model. Sci. Total Environ. 505, 939-951.

Williams, J.E., Le Bras, G., Kukui, A., Ziereis, H., and Brenninkmeijer, C.A.M., 2014. The impact of the chemical production of methyl nitrate from the $NO+CH_3O_2$ reaction on the global distributions of alkyl nitrates, nitrogen oxides and tropospheric ozone: a global modelling study. Atmos. Chem. Phys. 14(5), 2363-2382.

Willmott, C.J., 1982. Some comments on the evaluation of model performance. Bull. Am. Meteorol. Soc. 63(11), 1309-1313.

Zhang, L., Moran, M.D., Makar, P.A., Brook, J.R., and Gong, S., 2002. Modelling gaseous dry deposition in AURAMS: a unified regional air-quality modelling system. Atmos. Environ. 36(3), 537-560.